Identification of compounds that rescue otic and myelination defects in the zebrafish *adgrg6* (*gpr126*) mutant

Elvira Diamantopoulou[1,*], Sarah Baxendale[1,*], Antonio de la Vega de León[2], Anzar Asad[1], Celia J. Holdsworth[1], Leila Abbas[1], Valerie J. Gillet[2], Giselle R. Wiggin[3] and Tanya T. Whitfield[1#]

[1]Bateson Centre and Department of Biomedical Science, University of Sheffield, Sheffield, S10 2TN, UK

[2]Information School, University of Sheffield, Sheffield, S1 4DP, UK

[3]Sosei Heptares, Steinmetz Building, Granta Park, Cambridge, CB21 6DG, UK

*These authors contributed equally

[#]Corresponding author:

Tanya T. Whitfield: t.whitfield@sheffield.ac.uk

ORCID iD: 0000-0003-1575-1504

Key words: zebrafish, aGPCR, Adgrg6, Gpr126, phenotypic screening, chemoinformatics, *versican*, myelination, inner ear, lateral line, Schwann cells

ABSTRACT

Adgrg6 (Gpr126) is an adhesion class G protein-coupled receptor with a conserved role in myelination of the peripheral nervous system. In the zebrafish, mutation of *adgrg6* also results in defects in the inner ear: otic tissue fails to down-regulate *versican* gene expression and morphogenesis is disrupted. We have designed a whole-animal screen that tests for rescue of both up- and down-regulated gene expression in mutant embryos, together with analysis of weak and strong alleles. From a screen of 3120 structurally diverse compounds, we have identified 68 that reduce *versican b* expression in the *adgrg6* mutant ear, 41 of which also restore *myelin basic protein* gene expression in Schwann cells of mutant embryos. Nineteen compounds unable to rescue a strong *adgrg6* allele provide candidates for molecules that interact directly with the Adgrg6 receptor. Our pipeline provides a powerful approach for identifying compounds that modulate GPCR activity, with potential impact for future drug design.

INTRODUCTION

Adgrg6 (Gpr126) is an adhesion (B2) class G protein-coupled receptor (aGPCR) with conserved roles in myelination of the vertebrate peripheral nervous system (PNS) (reviewed in (Langenhan et al., 2016; Patra et al., 2014)). In homozygous loss-of-function *adgrg6* zebrafish and mouse mutants, peripheral myelination is severely impaired: Schwann cells associate with axons, but are unable to generate the myelin sheath, and show reduced expression of the *myelin basic protein* (*mbp*) gene (Glenn and Talbot, 2013; Mogha et al., 2013; Monk et al., 2009; Monk et al., 2011). Targeted disruption of *Adgrg6* in the mouse results in additional abnormal phenotypes, including limb and cardiac abnormalities, axon degeneration and embryonic lethality (Monk et al., 2011; Patra et al., 2014; Waller-Evans et al., 2010). In humans, mutations in *ADGRG6* are causative for congenital contracture syndrome 9, a severe type of arthrogryposis multiplex congenita (Ravenscroft et al., 2015). Peripheral nerves from affected individuals have reduced expression of myelin basic protein, suggesting that the function of ADGRG6 in myelination is evolutionarily conserved from teleosts to humans (Ravenscroft et al., 2015). Human *ADGRG6* variants have also been proposed to underlie some paediatric musculoskeletal disorders, including adolescent idiopathic scoliosis (Karner et al., 2015) (and references within).

In zebrafish, homozygous loss-of-function *adgrg6* mutants exhibit an inner ear defect in addition to deficiencies in myelination (Geng et al., 2013; Monk et al., 2009). In the otic vesicle, the epithelial projections that prefigure formation of the semicircular canal ducts overgrow and fail to fuse, resulting in morphological defects and ear swelling. Analysis of the zebrafish *adgrg6* mutant ear shows a dramatic alteration in the expression of genes coding for several extracellular matrix (ECM) components and ECM-modifying enzymes (Geng et al., 2013) (Fig. 1A). Notably, transcripts coding for core proteins of the chondroitin sulphate proteoglycan Versican, normally transiently expressed in the outgrowing projections and then down-regulated once projection fusion has occurred, remain highly expressed in the overgrown and unfused projections of *adgrg6* mutants (Geng et al., 2013). Although *Adgrg6* (*Gpr126*) mRNA is known to be expressed in the mouse ear (Patra et al., 2013), a role in otic development in the mammal has yet to be determined.

Like all aGPCR members, the zebrafish Adgrg6 receptor consists of a long extracellular domain (ECD), a seven-pass transmembrane domain (7TM), and a short intracellular domain (reviewed in (Langenhan et al., 2016)) (Fig. 1B). The ECD includes a GPCR autoproteolysis-inducing (GAIN) domain, which incorporates the GPCR proteolytic site (GPS) and the conserved Stachel sequence (Liebscher et al., 2014; Patra et al., 2014). Proteolysis at the GPS results in two fragments, an NTF (N-terminal fragment) and a CTF

(C-terminal fragment), which can remain associated with one another, or may dissociate, the NTF binding to cell surface or extracellular matrix ligands (Patra et al., 2014; Petersen et al., 2015). Dissociation of the NTF triggers binding of the Stachel sequence to the 7TM domain, thereby activating the CTF (Liebscher et al., 2014). This feature provides a variety of CTF-dependent or -independent signalling capabilities that orchestrate cell adhesion and other cell-cell or cell-matrix interactions. For example, during Schwann cell development and terminal differentiation, the Adgrg6 NTF promotes radial sorting of axons, while the CTF is thought to signal through a stimulatory Gα subunit ($G\alpha_s$), leading to elevated cAMP levels and activated protein kinase A (PKA) to induce transcription of downstream target genes, such as *egr2* and *oct6* (Petersen et al., 2015). Compounds that act to raise intracellular cAMP levels, such as the phosphodiesterase inhibitor 3-isobutyl-1-methylxanthine (IBMX) and the adenylyl cyclase activator forskolin, can rescue phenotypic defects in both the inner ear and PNS in *adgrg6* mutants (Geng et al., 2013; Monk et al., 2009).

Despite the enormous importance of GPCRs as drug targets (Hauser et al., 2017; Sriram and Insel, 2018; Wootten et al., 2018), adhesion class GPCRs remain poorly characterised, representing a valuable untapped resource as targets of future therapeutics (Hamann et al., 2015; Monk et al., 2015). The identification of specific modulators of aGPCR activity is an essential step for understanding the mechanism of aGPCR function and to inform the design of new drugs. Recent successful approaches include the use of Stachel sequence peptides as aGPCR agonists (Demberg et al., 2017), or synthetic monobodies directed against domains within the NTF (Salzman et al., 2017). A promising alternative approach lies in the potential of unbiased whole-animal screening of small molecules. In recent years, zebrafish have emerged as an important tool for in vivo phenotypic screening for new therapeutics (Brady et al., 2016) and for understanding biological mechanisms (Baxendale et al., 2017; Richter et al., 2017). Zebrafish have many advantages for drug discovery: they are a vertebrate species whose embryos can fit into individual wells of a multiwell plate, facilitating high-throughput analysis; they generate large numbers of offspring; they can absorb compounds directly added to the water, and whole-organism screening enables toxicity, absorption, metabolism and excretion of compounds to be assayed early in the screening pipeline.

To date, over one hundred drug screens using different zebrafish disease models have been conducted, some identifying lead compounds that have subsequently been tested in mammalian model systems or entered clinical trials (Chowdhury et al., 2013; Griffin et al., 2017; North et al., 2007; Owens et al., 2008) (reviewed in (Baxendale et al., 2017)). Two screens have been performed to identify compounds that promote myelination in the central

nervous system (Buckley et al., 2010; Early et al., 2018). These studies used live imaging of *Tg(olig2:GFP)* or *Tg(mbp:eGFP)* fluorescent transgenic lines to screen for small molecules that increase progenitor or myelinating oligodendrocyte cell number. While elegant in design, and successful in identifying hit compounds, these screens required the use of sophisticated and costly high-resolution imaging platforms and relied on detailed quantitative assays for cell number, techniques that are not available to all labs and are potentially limiting in scalability and throughput.

In this study, we have developed an in vivo drug screening assay based on semi-automated in situ hybridisation (ISH) to identify modulators of the Adgrg6 pathway. We have used the otic expression of *versican b (vcanb)* as an easily-scored qualitative readout to identify compounds that can reduce *vcanb* overexpression back to normal levels in a hypomorphic mutant allele for *adgrg6*, *tb233c*. We used expression of *mbp* in the posterior lateral line ganglion of *adgrg6*^{tb233c} mutants as a secondary screening assay, with the aim of identifying chemical classes capable of rescuing the expression of both genes, which may thus represent agonists of the Adgrg6 signalling pathway. To identify ligands that bind directly to Adgrg6, we then tested hit compounds for their ability to rescue a strong loss-of-function *adgrg6* allele, *fr24*, which predicts a severely truncated protein. Several compounds were unable to rescue *adgrg6*^{fr24} mutants, including a group with similar structures from the gedunin family of compounds. Compounds able to rescue both alleles include colforsin, a known activator of adenylyl cyclase, demonstrating proof-of-principle that our screen can identify compounds that restore GPCR pathway activity downstream of the receptor. These alternative assays for both down-regulation and up-regulation of gene expression, combined with a comparison of rescue in both weak and strong alleles, have facilitated selection of a strong cohort of hit compounds that can be differentiated by the different screens used. Our approach is scalable and can be used to screen additional compound collections. In parallel, chemoinformatics analysis of the compound libraries and identified hits has enabled classification and prioritisation of selected hit compounds.

RESULTS

Choice of markers for an in situ hybridisation-based screen: otic *vcanb* expression as a robust readout

We set out to develop a simple assay to identify small molecule modifiers of the Adgrg6 pathway that can be used both to understand Adgrg6 function and to identify compounds that could inform the design of therapeutics. To this end, we chose to perform a drug screen based on in situ hybridisation (ISH), which has the advantage of being a simple, reproducible assay that can be semi-automated (Baxendale et al., 2012; North et al., 2007). We selected *vcanb* expression in the *adgrg6* mutant ear for our primary screen. *vcanb* has a number of advantages for screening, including highly localised expression in the otic vesicle, very strong and reproducible staining intensity in *adgrg6* mutant embryos, and a clear difference between staining in mutant and wild-type embryos at the stage chosen, making it ideal for manual scoring (Fig. 1A). We therefore developed a primary screen seeking compounds that can reduce *vcanb* levels in *adgrg6* mutant embryos and rescue the mutant phenotype. We reasoned that, in addition to yielding information for the ear phenotype, compounds that can rescue *vcanb* expression may also rescue myelination defects in the PNS, where expression patterns of genetic markers are more complex and defects are harder to score.

We first made a careful comparison of the otic and PNS defects in weak (*tb233c*) and strong (*fr24*) alleles for the *adgrg6* mutant (Fig. 1A). The *tb233c* allele is a missense mutation (I963N) in the fourth transmembrane domain of the receptor, whereas the *fr24* allele is a nonsense mutation (L463X), predicting a severely truncated protein lacking the GAIN, 7TM and C-terminal domains (Geng et al., 2013) (Fig. 1B). Mutants for each allele have the same defect in semicircular canal formation: otic epithelial projections are enlarged, overgrow, and fail to fuse to form the three pillars that create the hubs of the semicircular canal ducts (Geng et al., 2013) (Fig. 1A). Time-lapse imaging using light-sheet microscopy reveals the dynamics of this process: even when projections make contact with each other, they fail to adhere as in the wild type. Instead, projections in the mutant ear continue to grow, roll around one another as they find space with least resistance, and fill the otic vesicle with semicircular canal projection tissue (Fig. 1C; Supplementary videos 1,2). In wild-type ears, *vcanb* is expressed in the growing semicircular canal projections between 44 and 72 hours post fertilisation (hpf), but is then strongly down-regulated after fusion; by 4 days post fertilisation (dpf), very little expression is detectable in the ear (Geng et al., 2013). By contrast, in *adgrg6* mutants, the overgrown and unfused projections in the developing ear continue to express *vcanb* at high levels (Geng et al., 2013) (Fig. 1A). Both alleles show a dramatically increased level of expression over wild-type embryos, but the increase is

stronger in the *fr24* allele (Fig. 1A). mRNA for *adgrg6* itself is expressed in mutant embryos for both alleles (Geng et al., 2013) (and unpublished data).

In addition to an upregulation of *vcanb* expression in the ear, the zebrafish *adgrg6* mutant also shows a reduction or loss of expression of the *myelin basic protein* (*mbp*) gene in the PNS (Geng et al., 2013; Monk et al., 2009). This additional phenotype proved to be very valuable for our screen design, helping to validate hits and eliminate false positives. Expression of *mbp* is present in a complex pattern in wild-type embryos, and shows clear differences between the two alleles, correlating with the predicted severity of the mutations (Fig. 1B). Expression is variably reduced along the posterior (trunk) lateral line nerve in homozygous mutants for the hypomorphic *tb233c* allele, but in all individuals there is consistent absence of staining in cells (presumed Schwann cells) associated with the posterior lateral line ganglion (PLLg) (Geng et al., 2013) (Fig. 1A). The *fr24* allele lacks nearly all *mbp* staining along peripheral nerves (Geng et al., 2013) (Fig. 1A). Note that expression of *mbp* in the central nervous system (CNS) is not affected in either allele, obscuring any reduction of *mbp* staining in the PNS without performing a detailed analysis. This made *mbp* expression unsuitable for a primary screen, but useful for a secondary screen of hit compounds identified from the *vcanb* screen.

Design of a screening pipeline for compounds that rescue the *adgrg6*^{tb233c} mutant phenotype

Our strategy for the screening protocol and analysis pipeline is outlined in Figure 2. Both the weak (*tb233c*) and strong (*fr24*) alleles of *adgrg6* mutants are homozygous viable, enabling large batches of 100% mutant embryos to be generated for each assay. We decided to use the hypomorphic allele (*tb233c*) in our primary screen, for four main reasons: (1) adult fish homozygous for the *tb233c* allele produce a larger number of healthy embryos than adults homozygous for the *fr24* allele; (2) a lower concentration of our positive control compound IBMX was sufficient to rescue the phenotype in *tb233c* mutants compared with *fr24* mutants (Geng et al., 2013), suggesting that the *tb233c* allele might also be easier to rescue with other compounds in the libraries screened; (3) *vcanb* expression, although not as dramatically affected as in *fr24*, is still robustly over-expressed in the *tb233c* allele, and (4) we predicted that any small molecules that interact with the active site of the receptor or act as allosteric modulators would be missed in a screen using *fr24* mutants, which should only be able to identify compounds acting on targets downstream of the receptor. By using *tb233c*, we should be able to identify modulators of the pathway acting both downstream and at the level of the receptor itself.

Choice of controls

In all assay plates, we included the phosphodiesterase inhibitor IBMX (100 µM) as a positive control. We have previously shown that addition of 100 µM IBMX at 60 hpf is optimal for both down-regulation of *vcanb* expression and a rescue of projection fusion in the ears of *adgrg6*^{tb233c} mutants (Geng et al., 2013). At this stage of development, the anterior and posterior projections in the mutant otic vesicle are extended and in close proximity to the lateral projection, to which they would fuse in the wild type (Fig. 2A). Compounds from both libraries are supplied as stocks dissolved in DMSO; we therefore used 1% DMSO as a negative control. The *nacre* (*mitfa*$^{-/-}$) strain, which has reduced pigmentation, facilitating visualisation of ISH staining patterns, was used as an untreated wild-type control. Three embryos per well were treated with compounds at 25 µM in E3 medium from 60–90 hpf, after which they were fixed and analysed for expression of *vcanb* by whole-mount ISH. At the embryonic stage assayed by ISH (90 hpf), expression of *vcanb* in untreated mutant embryos is very specific to the ear, making it clearly visible as two dark spots in the head of each embryo within the well. All controls gave results as expected in all assay plates tested: DMSO-treated mutant embryos showed strong otic staining for *vcanb*, untreated wild-type embryos showed very little staining in the ear, and IBMX-treated mutant embryos showed rescued (down-regulated) otic *vcanb* expression (Fig. 2A).

Comparison of compound libraries with diverse structures

In order to test a wide range of compounds, we chose to screen two commercial small molecule libraries. The Tocriscreen Total library ('Tocris') consists of 1120 compounds representing known bioactive compounds with diverse structures. The Spectrum Collection ('Spectrum'; Microsource Discovery Systems) comprises 2000 compounds, including FDA-approved drugs for repurposing, bioactive compounds and natural products. Scaffold analysis of the two libraries highlights the structural diversity present (Fig. 3—Supplemental file 1). Based on Bemis-Murcko scaffolds (Bemis and Murcko, 1996), the Tocris library of 1120 compounds has 693 (62%) scaffolds representing a single compound and only two scaffolds representing more than 10 compounds. The Spectrum library has 682 scaffolds representing unique chemical structures, but as the library consists of 2000 compounds, the proportion of scaffolds represented by a single molecule (30%) is lower than for the Tocris library. Together, the two libraries cover a wide range of chemical space, with a total of 1540 scaffolds, of which 1134 represent unique compounds. Scaffold analysis not only provides a broad overview of the chemical diversity of each library, but can also be used to select and analyse groups of similar compounds with interesting structure-activity relationships. Compounds were also clustered based on their fingerprint similarity using

Ward's method of hierarchical agglomerative clustering, which was useful for visualisation purposes (for dendrograms, see Fig. 3—Supplemental file 2).

Results of the primary screen for reduction of otic *vcanb* expression levels

To score the efficacy of the compounds in down-regulating *vcanb* mRNA levels, we used a scoring system from 0 to 3 (Fig. 3; for details, see the Materials and Methods). In the primary screen, each compound was tested against three embryos and the score for each embryo was added to give a final score out of 9. The final scores were classified into different groups according to the thresholds shown in Figure 3B, with the highest degree of rescue in Category A, representing a combined score no greater than 2. Completion of the primary *vcanb* screen for all 3120 compounds identified 92 (8%) compounds from the Tocris library and 205 (10%) from the Spectrum library that scored in categories A–C (Fig. 3C,E). 5% of the compounds from each library were found to be either toxic (category F; dead embryos or severe developmental abnormalities) or potentially corrosive (category G; no embryos present), while 99 (9%) compounds from Tocris and 269 (13%) from Spectrum were found to cause incomplete or partial suppression of *vcanb* expression (category D). The largest category (E; 2282 compounds from both libraries, 73%), as expected, represented compounds that had no rescuing or other effect at the concentration used (25 µM). To visualise the complete set of screening results and to identify any clusters of hit compounds with similar structures, compounds were displayed as individual data points on a polar scatterplot (Fig. 3D,F; Fig. 4; interactive version at https://adlvdl.github.io/visualizations/polar_scatterplot_whitfield_vcanb.html). Compound position along the circumference of the plot for each library is based on position on the respective similarity dendrogram (Fig. 3—Supplemental file 2). Data points that are clustered along radii of the plot are thus more likely to be structurally similar, although note that the juxtaposition of different branches of the dendrogram can also place compounds that differ in structure adjacent to one other. Due to the wide diversity of scaffolds found in the Tocris library, less clustering of hit compounds (A–C) can be observed compared with the molecules in the Spectrum library, where more clusters of compounds in the A–C categories are evident (Fig. 3D,F).

Validation of the primary screen: retesting, comparison with control compounds and analysis of duplicates

A large subset of the possible hit compounds categorised as A–C were selected and arrayed in a cherry-picked plate, which was tested using the same assay format. These included all the top hit compounds that scored A or B, and a selection of compounds from the lower-scoring C category. Specifically, 83 out of the 92 possible hit compounds from the Tocris

library and 145 of the 205 possible hits from the Spectrum library were retested twice, again with three embryos per well. By increasing the number of embryos screened to a total of nine per compound, we aimed to eliminate any false-positive hits that had an increased average score over these two retests. In addition, after each retest, any compounds that did not show a clear rescue (score >7) were not followed through to the next stage. In total, 91 compounds from the combined list of hits (29 from Tocris, 62 from Spectrum) that showed consistent rescue of *vcanb* expression across the retests were taken forward for secondary assays (Supplemental Table S1).

To evaluate the success rate of the hit compound selection process, we compared the hits in each original category with the final category based on the average score for the nine embryos (and in a few cases, six embryos). We were interested to know if the hits in the original C category were less likely to be selected after the retest and therefore by choosing a threshold of A or B scores we were choosing the strongest hits. We found that of the 191 hit compounds that originally scored A or B, 184 rescreened with a score of A–C, and 7 compounds showed some toxicity (Fig. 4A–C). In comparison, of the 33 compounds with an original C score that were retested, 9 scored as B or C, 23 scored as D, and one compound scored as F (toxic). Thus, for our assay, >60% of potential hits with an original C score did not pass a hit threshold in the retest, whereas >96% of hits with an original A or B score were selected again in the retests.

To provide further validation for the hits identified in the primary screen, we used two approaches. Firstly, we compared the results of our control compounds to those of similar compounds present in the screened compound libraries. The control compound IBMX, a non-selective phosphodiesterase (PDE) inhibitor, is present in the Spectrum library and was identified as a hit in the primary screen (Fig. 2A). The most similar compound to IBMX from both libraries is 8-methoxymethyl-3-isobutyl-1-methylxanthine (MMPX), a selective PDE-1 inhibitor. MMPX is present in the Tocris library, but was not identified as a hit in our screen, most likely due to its selectivity. In previous work we also used forskolin to raise cAMP levels and rescue the *adgrg6* ear phenotype (Geng et al., 2013), but forskolin requires different assay conditions with short drug incubation times to avoid toxicity. Forskolin is represented in the Tocris library, but was toxic in our screening assay. The Spectrum Collection contains two forskolin-related compounds, colforsin and desacetylcolforsin. Colforsin, a water-soluble derivative of forskolin, was identified as a hit in the primary screen, and retested positive in all subsequent tests (see also below); it appeared to be less toxic than forskolin, whereas desacetylcolforsin was toxic at the concentration used. The

identification of both IBMX and colforsin as hits in the primary screen confirmed that the assay conditions used were efficient at detecting expected hit compounds.

Secondly, we compared the scores for all compounds that were duplicated in both compound libraries. Chemoinformatics analysis of the Tocris and Spectrum libraries identified 155 compounds represented in both libraries, 65% of which (100/155) had exactly the same *vcanb* score average from the two individual screens. 39 (25%) of the 155 duplicate compounds yielded a *vcanb* score average that differed by 1–2 units between the two libraries; 12 (8%) of the compounds yielded a *vcanb* score average that differed by 3–6 units, while only 4 (3%) compounds had a score average that differed by 7–9 units. In summary, 90% (139/155) of the compounds common to both libraries showed similar scores for the *vcanb* assay from each library (scores differing by ≤2 units), while 10% (16/155) of the compounds resulted in differing levels of *vcanb* down-regulation between the two different libraries. After retesting, the difference between the two *vcanb* score averages for nine of these compounds was reduced; however, for seven compounds, the scores between the two libraries remained significantly different. These discrepancies could be either due to differences in compound purity between the two suppliers, or could be due to experimental error (e.g. in the concentration used, or during the ISH protocol). In cases where the same compound was scored as toxic in one assay and not in another, the health condition of the fish in a particular well could be the underlying reason. Duplicated compounds have been included in the data for each library in the polar scatter plots (Figs 3,4).

The top 91 hit compounds from both libraries (29 from Tocris, 62 from Spectrum) that scored A–C in all three *vcanb* assays were combined to give a complete list of 89 unique compounds, with baicalein and gedunin present in both libraries. The list covers a wide spectrum of naturally-derived and synthetic molecules, with known and unknown functions (Supplementary Table S1). The hit compounds with known functions include calcium channel blockers, antifungal, anti-inflammatory, antihyperlipidemic, antibacterial and anthelmintic agents, as well as compounds with known antineoplastic and vasodilatory properties.

Secondary screen for rescue of *mbp* expression, and identification of false positives

The two retests for *vcanb* expression significantly reduced the possibility of false-positive results due to experimental error (e.g. in the ISH protocol), but the list of hits could still contain false-positive compounds that may generally inhibit transcription or cause developmental arrest of the embryo. In order to eliminate such compounds, we exploited the expression of *mbp* as a secondary screening assay, testing for rescue of expression in

the posterior lateral line ganglion (PLLg) and from three small regions near the cristae of the inner ear (Fig. 4D; Materials and Methods). This counterscreen has the advantage of assessing for up-regulation (restoration) of *mbp* expression in mutant embryos, in contrast to the down-regulation of *vcanb* expression in the primary screen. All compounds that passed the first retest for *vcanb* (89 compounds in total) were subjected to this secondary assay for *mbp* expression. We used the same assay format and treatment time window as for *vcanb*, as we had previously found that treatment with IBMX between 60 and 90 hpf was also able to rescue *mbp* expression in *adgrg6* mutants (not shown).

Following two experimental repeats (*n*=6 fish tested per drug), compounds were categorised into groups based on their average *mbp* score. These included groups of compounds that showed rescue of the mutant phenotype (an increase of *mbp* expression, specifically in the PLLg); no rescue (*mbp* expression equivalent to that in untreated *adgrg6*^{tb233c} mutants), and those that resulted in a decrease in *mbp* expression, as shown in Figure 4D. We identified 41 compounds (12 from Tocris, 29 from Spectrum) that rescued *mbp* expression and thus represent possible modulators of Adgrg6 pathway (Fig. 4E,F; Table 1). Twenty-eight hit compounds (15 from Tocris, 13 from Spectrum) strongly down-regulated *vcanb* expression but did not affect *mbp* expression in *adgrg6*^{tb233c} mutants. These could represent compounds that can rescue *vcanb* expression in an inner ear-specific or Adgrg6-independent manner. Alternatively, as all the assays were carried out at a single concentration (25 µM), it is possible that some or all of these compounds could rescue *mbp* expression at a higher concentration (as is the case for IBMX with the *fr24* allele). The 28 members of this group are structurally and functionally diverse (Supplementary Table S1). Finally, 22 compounds (2 from Tocris, 20 from Spectrum) reduced the expression of both *vcanb* and *mbp.* This latter group—potential false positives in the *vcanb* assay—could represent general inhibitors of transcription or development, and were excluded from further analysis, resulting in a final list of 68 hit compounds (Supplementary Table S1).

Compounds that can rescue both inner ear and myelination defects

The 41 compounds that could both down-regulate *vcanb* expression and restore *mbp* expression to wild-type levels in *adgrg6*^{tb233c} mutants, presumed modulators of the Adgrg6 signalling pathway (Table 1), are highlighted on the final combined polar scatter plot (Fig. 4G). Although hit compounds are scattered around the plot, some clustering is evident, and we chose two groups for further analysis (Fig. 4G; boxes at 300, 2500). These groups with five or more compounds included the pyridines (cluster 1 on the scatter plot) and the tetranortriterpenoids (gedunin derivatives) (cluster 2 on the scatter plot). The pyridine cluster included one pyrazolopyridine and six dihydropyridines, a class of L-type calcium

channel blockers with vasodilatory properties (reviewed in (Tocci et al., 2018)). The gedunins are a family of naturally occurring compounds, previously attributed with antineoplastic and neuroprotective effects (Jang et al., 2010; Subramani et al., 2017).

Data from each of the screens and retests were used to cluster the compounds into groups based on their activity (displayed as a heat map in Fig. 5A), and compared with a compound network display based on structural similarity in Fig. 5B; interactive version at https://adlvdl.github.io/visualizations/network_whitfield_vcanb_mbp/index.html). A selection of compounds was chosen for further study (Figs 6–8). As many of the compounds classified as putative Adgrg6 pathway modulators were dihydropyridines (cluster 1, Fig. 4), two compounds were chosen from this class for further study (cilnidipine and nifedipine). The third compound that was chosen was tracazolate hydrochloride, a pyrazolopyridine derivative belonging to the nonbenzodiazepines and a known γ-aminobutyric acid A ($GABA_A$) modulator (Thompson et al., 2002), which strongly down-regulated *vcanb* expression to wild-type levels. FPL 64176 was also chosen for further analysis, based on its potent efficacy in down-regulating *vcanb,* and the fact that it was the only calcium channel modulator (Liu et al., 2003) that did not rescue *mbp* expression efficiently. Initial experiments to repeat the rescue of the *vcanb* and *mbp* expression with freshly-sourced compounds from alternative suppliers (see Materials and Methods) confirmed that the pyridines cilnidipine, nifedipine and tracazolate hydrochloride were able to decrease otic *vcanb* expression and increase *mbp* expression in the PLLg in mutant embryos for the *tb233c* allele, whereas FPL 64176 was able to reduce *vcanb* expression but was unable to restore *mbp* expression to wild-type levels (Fig. 6C).

Nifedipine, cilnidipine, tracazolate hydrochloride and FPL 64176 rescue otic defects in *adgrg6*^{tb233c} mutants in a dose-dependent manner

The four compounds shown in Figure 6 were also selected for dose-response assessment, by exposing *adgrg6*^{tb233c} embryos to concentrations ranging from 0.3 μM to 222.2 μM between 60–110 hpf. Nine embryos were tested for each concentration, and a 1.5-fold dilution series of each drug was used. ISH analysis of the 110-hpf embryos revealed a robust, dose-dependent down-regulation of *vcanb* mRNA expression in response to treatment with all four drugs (Fig. 7). Expression of *vcanb* mRNA was assessed by annotating each embryo with two scores, one representing the intensity of the stain (score as in Fig. 3A) and the other representing the number of projections stained (Fig. 7A). All four drugs were able to reduce both the intensity of the ISH staining and the number of projections stained in the ear in a dose-dependent manner. For each of the four drugs, the

intensity of the *vcanb* staining decreased even after treatment with low doses, whereas higher doses were needed to reduce the number of the projections stained.

In order to investigate whether other aspects of the ear phenotype in *adgrg6*^{tb233c} mutants could be rescued by compound treatment, the inner ears of live treated embryos were observed with differential interference contrast (DIC) optics at 110 hpf (or 90 hpf in the case of FPL 64176, due to its toxicity). Consistent with the *vcanb* scores for the number of projections stained, live DIC images of the inner ear revealed a dose-dependent rescue of projection fusion and pillar formation, which was greater at higher doses (Fig. 7). As *adgrg6*^{tb233c} mutants have a swollen ear phenotype (Geng et al., 2013), measurements of the ear-to-ear width, normalised for size differences between individuals, were taken from photographs of live embryos mounted dorsally. The results showed a dose-dependent reduction in ear swelling with increased concentration of the four drugs (Fig. 7C; Fig. 7—Supplemental file 1). LD50 concentrations were also determined for each of the four compounds and ranged from 19.2 μM (cilnidipine) to 51.7 μM (tracazolate hydrochloride) (Fig. 7—Supplemental file 2).

Test for rescue of *vcanb* expression in the *fr24* allele: screen for Adgrg6-specific ligands

The initial screen was performed on the hypomorphic *tb233c* allele. We differentiated our hit compounds further by re-screening for *vcanb* expression in a strong *adgrg6* allele, *fr24* (Fig. 1B), to identify compounds that could potentially interact directly with the Adgrg6 receptor itself. We predicted that any compounds able to rescue both alleles (such as IBMX at higher concentrations) are likely to act downstream of the receptor. On the other hand, hits that rescued *tb233c*, but were not able to rescue *fr24,* are likely to act as putative agonistic ligands for the Adgrg6 receptor. Of the 41 hit compounds able to rescue both *vcanb* and *mbp* in the *tb233c* allele, we identified 10 compounds that also rescued *vcanb* expression in the *fr24* screen (score sum 0–7 in Table 1, yellow), 12 compounds that gave a partial or inconclusive rescue (white), and 19 compounds that did not affect *vcanb* expression in the *fr24* screen (score sum 9 in Table 1, grey). The first group (yellow) are presumed to act downstream of the Adgrg6 receptor, and include colforsin, which tested positive in all assays and is a known activator of adenylyl cyclase, supporting this interpretation (Fig. 8). The last class (grey) are of particular interest as they represent candidates for molecules that interact directly with the receptor. Examples of the difference in ability to rescue the two *adgrg6* alleles between the two classes can be seen in Figure 8C.

Interestingly, four of the 19 compounds in the last group are in the cluster of gedunin derivatives identified in Figure 4 (cluster 2), with deoxygedunin being one of the top ten most potent drugs able to rescue the *tb233c* allele. The compound network shows that 38 compounds with structural similarity to the gedunins are represented in the two libraries (Figs 5,8). In the primary screens, 25/38 (66%) gedunin-related compounds affected *vcanb* expression to some extent (18 compounds in categories A–C and 7 in D), 9 compounds were inactive and 4 were toxic. The majority of the gedunin-related compounds that passed both rounds of retesting were later found also to rescue *mbp* expression (8/10, 80%). The shared structural characteristics of the gedunin group may give useful clues for candidate structures of agonistic ligands for Adgrg6. In summary, our study demonstrates a novel screening approach which, when combined with chemoinformatics analysis, is able to delineate both expected downstream rescuers of the Adgrg6 pathway and several candidates for drugs that may interact directly with the Adgrg6 receptor.

DISCUSSION

Adhesion GPCRs are critical regulators of development and disease, driving cell-cell and cell-ECM communications to elicit internal responses to extrinsic cues. This study set out to identify positive modulators of the Adgrg6 signalling pathway, a key regulator of myelination and inner ear development in the zebrafish embryo. Use of a whole-animal phenotypic (mutant rescue) screen gave the potential to identify compounds affecting the entire Adgrg6 pathway in the correct cellular context. We have used a simple in situ hybridisation approach to assay *vcanb* expression in the inner ear of *adgrg6* mutants, exploiting an easily identifiable phenotype that could be scored manually. Following our primary screen of 3120 small molecules, we tested 89 hit compounds in a counter screen for rescue of the myelination defect in *adgrg6* mutant embryos. We identified 41 compounds that can both rescue *vcanb* expression in the inner ear and *mbp* expression in Schwann cells of *adgrg6* hypomorphic mutants, suggesting these are Adgrg6 pathway-specific modulators. Further analysis of a strong *adgrg6* allele, *fr24*, identified a subset of 19 compounds that are potential direct interactors of the Adgrg6 receptor. This analysis, combined with chemoinformatics analysis of the identified hit compounds, has identified clusters of compounds acting at different levels of the Adgrg6 pathway.

An optimal drug screening assay design identifies the maximum number of hit compounds with the minimum number of false positives and false negatives. Chemical screening assays using zebrafish range from simple morphology screens (Yu et al., 2008) through to high-tech, automated methods for quantitative image analysis (Early et al., 2018) or behavioural analysis (Bruni et al., 2016; Rennekamp et al., 2016) (reviewed in (Kalueff et al., 2016)). We used an in situ hybridisation screen to analyse gene expression changes, as this has the advantages of being scalable to different sized projects and relatively inexpensive to perform—with results that are stable and reproducible. Spatial resolution of staining patterns can be accurately scored: expression pattern screens have recently been used to identify small molecules that can induce subtle differences in gene expression domains along the pronephros (Poureetezadi et al., 2016) and in the somites (Richter et al., 2017). Although quantification of gene expression levels is less reliable with an enzymatic reaction compared with a fluorescent signal, we utilised the strong contrast between the high *vcanb* expression in the ear of *adgrg6* mutant fish compared with the low expression in a small dorsal region of the wild-type ear at 4 dpf to produce a robust scoring system for our phenotype rescue.

Relatively few zebrafish screens have been undertaken to identify compounds that can increase myelination (Buckley et al., 2010; Early et al., 2018) or restore myelination in

neuropathy models (Zada et al., 2016), which is in part due to the complex distribution of glial cells in both the CNS and PNS. Performing the primary screen using our ear marker, *vcanb*, enabled us to bypass the difficulties of scoring and quantification of *mbp* staining on a large scale; instead, *mbp* expression was used as a counter screen on a limited number of cherry-picked hits. Contrary to the primary assays, which screened for down-regulation of *vcanb* expression, the counter screen assayed for up-regulation of *mbp* expression, enabling the identification of 21 false-positive compounds that down-regulate the expression of both genes (presumably by inhibiting transcription).

Determining the false-negative rate for any screen is difficult. In our assay we used only one concentration of compound (25 µM), so it is likely that we missed compounds that were toxic or where the dose was suboptimal; these may be effective at different concentrations. One possibility would be to run a parallel screen at a lower or higher concentration or use an alternative protocol with shorter incubation times, an approach that has recently proved successful at identifying different compounds influencing segmentation in zebrafish (Richter et al., 2017). Here, the compounds were found to be most active in the range of 10–50 µM, supporting our choice of 25 µM for the primary screen. However, increasing the number of replicates with different drug concentrations or assay conditions has significant implications on the cost and time taken to complete the screen, reducing the number of compounds analysed and the potential hits identified. Our minimum estimate for the false-negative rate is 5%, based on the seven compounds (out of a total of 155) that were duplicated in both libraries and had a significantly different score after retesting, being classified as a hit in one library but not in the other. It is possible that this is due to differences in chemical purity from the different suppliers. Other false-negative compounds could include those that are unable to penetrate into the ear. Neomycin, for example, is toxic to the superficial hair cells of the lateral line system, but is ineffective on inner ear hair cells unless microinjected into the ear (Buck et al., 2012). Other compounds that we will have missed could include myelination-specific compounds, as the primary assay scored for the ear phenotype only. Given that several compounds were positive hits for the rescue of *vcanb* in the ear and negative for *mbp*, it is likely that tissue-specific functions of Adgrg6 are mediated through different downstream pathways or are stimulated by different ligands.

Our positive control compound, IBMX, was identified independently through our screen as a category A hit. The hit compound colforsin was found to be more potent and less toxic than the related control compound forskolin, and had the highest score in every assay, showing full rescue of our strongest *fr24* allele. Both these observations highlight the robustness of the assay and the consistency of the scoring process. In total, the final number of hit

compounds identified was similar in both the compound libraries screened, with 42 compounds identified from the Spectrum library (2.1%) and 27 compounds from the Tocris library (2.4%). These hit rates are comparable to those found in other similar screens (Baxendale et al., 2012; Vettori et al., 2017). Chemoinformatics analysis and visualisation of the results provided additional context to the identified hit compounds. The polar scatter plot displayed an initial overview of the results and allowed the identification of clusters of active compounds with similar structure. The compound network focused the analysis on highly detailed similarity relationships inside each compound cluster, yielding a wealth of structure-activity relationship information that could prove very useful for any future optimisation of the identified hit compounds.

Of the 41 hit compounds able to rescue both inner ear and myelination phenotypes, 23 are grouped in six different structurally-related clusters. Seven of the 41 hit compounds that rescued *vcanb* and *mbp* expression are Ca^{2+}-channel modulators. Six of these (nifedipine, cilnidipine, nitrendipine, nimodipine, efonidipine, niguldipine) belong to the chemical group of dihydropyridines (cluster 1), some of which have neuroprotective effects in murine models. Nimodipine, for example, has been shown to trigger remyelination in a mouse model of multiple sclerosis and to improve repair in peripheral nerve crush injuries in rats (Schampel et al., 2017; Tang et al., 2015). As dihydropyridines have been reported to inhibit cAMP phosphodiesterases (Sharma et al., 1997), protection of cAMP from degradation might be another mechanism whereby these molecules exert their ameliorating action on the *adgrg6* mutant phenotype.

Phenotypic screens are advantageous for assessing models of multifactorial pathological conditions, such as hereditary neuropathies and cancer (reviewed in (Baxendale et al., 2017)). However, one of the challenges for phenotypic screening is the identification of the specific target for any hit compound, as multiple pathways and different cell types can contribute to a positive read-out in the screening assay. Our aim was to identify compounds that are likely to interact directly with the Adgrg6 receptor. We were able to separate hit compounds into different groups based on their ability to rescue otic phenotypes caused by missense (*tb233c*) and nonsense (*fr24*) mutations. In total, we found 19 hits that could rescue *vcanb* expression and *mbp* expression in the *tb233c* allele, but were unable to rescue the *fr24* allele. We hypothesise that the *fr24* allele is unable to produce the full-length Adgrg6 protein, and therefore any compounds that interact directly with the receptor would not be able to rescue this strong allele. Further analysis will be needed to determine whether any of these compounds can bind directly to the Adgrg6 receptor. However, this approach of using a combination of null and hypomorphic alleles in zebrafish whole-

595 organism screening with the aim of identifying target-specific compounds is particularly
596 exciting and one that the advent of CRISPR/Cas9 technology is placed to take full
597 advantage of, since it is now possible to generate designer mutations in the zebrafish
598 through homology-directed repair (Hruscha et al., 2013; Hwang et al., 2013; Komor et al.,
599 2016).
600
601 It is of interest to note that one of the main groups of compounds identified as potential
602 interactors of the receptor in the *fr24* screen is a cluster of gedunin derivatives (cluster 2).
603 One of these compounds, deoxygedunin, has previously been identified as a TrkB agonist
604 that has neuroprotective properties (Nie et al., 2015), can promote axon regeneration after
605 nerve injury (English et al., 2013), and, interestingly, has been found to protect the vestibular
606 ganglion from degeneration in mice mutant for *BDNF* (Jang et al., 2010). More recently,
607 gedunin derivatives, including 3-α-DOG, have been shown to act as partial agonists for the
608 closely related aGPCR, ADGRG1 (formerly GPR56) (Stoveken et al., 2018), a key regulator
609 of myelination in both the CNS and PNS (Ackerman et al., 2015; Ackerman et al., 2018;
610 Giera et al., 2015; Salzman et al., 2016). While further work will be necessary to determine
611 if gedunin-type molecules can also bind and activate zebrafish Adgrg6 by interacting directly,
612 these studies set a precedent for this type of interaction.
613
614 GPCRs can be modulated by the membrane lipid cholesterol, where interactions with the
615 7TM domain can provide plasticity for the receptors by altering their stability and structure
616 (Huang et al., 2018; Prasanna et al., 2016). In addition, cholesterol can activate the
617 hedgehog signalling pathway directly by binding to the extracellular domain of the GPCR
618 Smoothened (Huang et al., 2018; Luchetti et al., 2018). Although cholesterol was not
619 identified as a hit in our primary screen, we did identify two cholesterol-lowering drugs,
620 ezetimibe (Altmann et al., 2004) and rosuvastatin (Istvan and Deisenhofer, 2001), as
621 putative modulators of the Adgrg6 pathway. Whether these act by altering the activity of
622 Adgrg6 through altering cholesterol levels remains to be determined.
623
624 In addition to the dihydropyridines (cluster 1) and the tetranortriterpenoid (gedunin-derived)
625 compounds (cluster 2), there are also clusters of steroid hormones (danazol,
626 hydroxyprogesterone, pregnenalone succinate, hydrocortisone hemisuccinate) and flavonoid
627 compounds (baicalein, tangeritin, nobiletin, dimethylnobiletin, hexamethylquercetagetin).
628 The flavonoids are a group of molecules with wide ranging activities, including anti-cancer
629 (Ma et al., 2015) and neuroprotective properties (reviewed in (Braidy et al., 2017)). All four
630 *O*-methylated flavonoids that rescued *vcanb* and *mbp* expression in *tb233c* mutants were

also able to rescue *fr24* allele in our assay, suggesting that they act downstream of the Adgrg6 receptor.

Our screen identified 28 compounds that down-regulated *vcanb* expression but did not rescue *mbp* expression, which may provide useful tools to manipulate semicircular canal formation in vivo. Versican and other chondroitin sulphate proteoglycans (CSPGs) are associated with a number of human pathologies; Versican overexpression has been shown to be strongly involved in inflammation, cancer progression and the development of lung disorders (reviewed in (Andersson-Sjöland et al., 2015; Ricciardelli et al., 2009; Wight et al., 2017)). CSPGs and hyaluronan are components of the inhibitory scar that forms at the site of injury after CNS damage, preventing axon regeneration (Silver and Miller, 2004). In addition, CSPGs have been shown to inhibit the ability of oligodendrocytes to remyelinate axons, a process that is reversed by reduction of CSPG levels (Keough et al., 2016; Pendleton et al., 2013). Whether the down-regulation of CSPGs to promote remyelination occurs via a similar mechanism to that involved in Adgrg6-regulated projection fusion remains to be determined. However, it is of interest that a key regulator of myelination, Adgrg1, has also been recently shown to reduce fibronectin deposition and inhibit cell-ECM signalling to prevent metastatic melanoma growth (Millar et al., 2018).

In conclusion, our data show that *vcanb* expression in the *adgrg6*^{tb233c} mutant ear provides a robust, easy-to-use screening tool to identify drugs that target the Adgrg6 pathway. In combination with the different alleles available for *adgrg6* in zebrafish, this in vivo platform provides an excellent opportunity to find hit compounds specific for Adgrg6 in counter screens. These may provide a starting point for the development of therapeutic approaches towards human diseases where *ADGRG6* or myelination is affected. We have identified groups of structurally-related compounds that can rescue *adgrg6* mutant defects, including those that are likely to act downstream of the Adgrg6 pathway, and others that are candidates for interacting with the Adgrg6 receptor. The chemical analysis and structural comparison of the compounds shown to be putative Adgrg6 receptor agonists will contribute to the elucidation of the physical properties responsible for ligand binding and will provide further insight on the underlying mechanism of Adgrg6 signalling.

MATERIALS AND METHODS

Animals

Standard zebrafish husbandry methods were employed (Westerfield, 2000). To facilitate visualisation of in situ hybridisation (ISH) staining patterns, embryos of the *nacre* (*mitfa*$^{w2/w2}$) strain (ZDB-GENO-990423-18), which lack melanophores (Lister et al., 1999), but are phenotypically wild-type for expression of *vcanb* and *mbp*, were used as controls for all drug screening experiments. The wild-type strain used for dose-response experiments was London Wild Type (LWT). *adgrg6* mutant alleles used were *lau*^{tb233c} (formerly *bge*^{tb233c}) and *lau*^{fr24} (ZDB-GENE-070117-2161) (Geng et al., 2013; Whitfield et al., 1996), and were raised on a pigmented background. In all cases shown, mutant embryos are homozygous for the respective allele. The transgenic strain used for imaging in Fig. 1 and in the Supplemental movie was *Tg(smad6b:GFP)*, a gift of Robert Knight (Baxendale and Whitfield, 2016). Prior to treatment, embryos were raised in E3 embryo medium (Westerfield, 2000) at 28.5°C. We have used the term embryo throughout to refer to zebrafish embryos and larvae from 0–5 days post fertilisation (dpf).

Compound library storage, aliquoting and administration to embryos

Chemical compounds from the Tocriscreen Total library (Tocris, 1120 compounds) and The Spectrum Collection (Microsource Discovery Systems, 2000 compounds) were arrayed in MultiScreen-Mesh 96-well culture receiver trays (Millipore) in columns 2–11 and diluted to 25 µM in E3 medium for drug screening. Control wells contained either IBMX (3-isobutyl-1-methylxanthine, Sigma, 50 µM and 100 µM), DMSO (Sigma, 1% in E3) or E3, in columns 1 and 12 (see diagram of the plate layout in Fig. 2). Wild-type (LWT and *nacre*) and homozygous *adgrg6*^{tb233c} mutant embryos were raised to 50 hpf at 28.5°C in E3 medium, dechorionated manually with forceps, and then incubated at 20°C overnight to slow down development and facilitate timing of experimental treatments. This regime reduced ear swelling, but did not reduce otic *vcanb* levels, in mutant embryos. Embryos at the 60 hpf stage were aliquoted at three embryos per well into MultiScreen-Mesh mesh-bottomed plates (Millipore) and transferred to the drug plate (receiver tray; see above). Assay plates were incubated at 28.5°C for 28 hours and the embryos were then transferred to 4% paraformaldehyde and stored at 4°C overnight. Embryos were bleached according to the standard protocol (Thisse and Thisse, 2008) and stored at -20°C in 100% methanol until required for ISH. Hits identified in the primary screen were rescreened using the same protocol.

Scoring systems for *vcanb* and *mbp* expression

To score the efficacy of the drugs in down-regulating *vcanb* mRNA levels, a scoring system from 0 to 3 was used, with 0 being the score for a very efficient drug (a 'hit') that can suppress *vcanb* expression back to almost wild-type levels, and 3 the score for a drug that did not have any effect on *vcanb* mRNA levels expressed in the mutant ear. Scores 1 and 2 were given to drugs that showed an ability to down-regulate *vcanb* expression to some extent, with 1 given for a stronger down-regulation than 2 (Figure 5.2A). Drugs were then classified into categories A–E, according to the combined score from the three embryos treated with each drug (Figure 5.2B). Drugs categorised as A, B or C were considered successful, and were cherry-picked into new drug assay plates for further testing. Drugs categorised as D and E were considered to show incomplete or no inhibition of *vcanb* expression, respectively. Drugs from category F caused severe developmental abnormalities, heart oedema, brain oedema or death at the end of the treatment and therefore were characterised as toxic. Category G represented drugs that were potentially corrosive, as no fish were found in these wells at the end of the treatment, although this could also have resulted from death of the embryos followed by digestion by microorganisms, or through experimental error. Drugs that fell into any of the categories D–G were eliminated from the assay and were not followed further.

For the *mbp* counter screen (Fig. 4D,E), a score of 3 was used for embryos where *mbp* mRNA expression was rescued to wild-type levels, a score of 2 for embryos that showed some *mbp* expression in the PLLg (weaker than wild-type levels) and a score of 1 in cases where the *mbp* expression was identical to the one seen in untreated *adgrg6*^{tb233c} mutants (i.e. lacking *mbp* expression in the PLLg). The fact that *mbp* expression is not missing altogether from other areas of the PNS in *adgrg6*^{tb233c} mutants allowed us to use a score of 0 in cases where *mbp* expression levels were lower than those typically seen in *adgrg6*^{tb233c} mutants.

Whole-mount in situ hybridisation analysis of gene expression

Digoxigenin-labelled RNA probes for *vcanb* (Kang et al., 2004) and *mbp* (*mbpa*) (Brösamle and Halpern, 2002) were prepared as recommended (Roche). Whole-mount ISH was performed using standard procedures (Thisse and Thisse, 2008), modified for the Biolane HTI 16V in situ robot (Intavis) and MultiScreen-Mesh mesh-bottomed plates to increase throughput (Baxendale et al., 2012). Stained embryos were scored manually by at least two people and any discrepancies between the results were re-analysed.

Dose-response and LD50 assays

Selected compounds were purchased separately from Sigma (nifedipine and cilnidipine), Cayman Chemicals (FPL 64176) and Santa Cruz Biotechnology (tracazolate hydrochloride) for testing in dose-response assays. In order to assess the ear swelling in drug-treated *adgrg6*^{tb233c} mutant embryos, the ear-to-ear width was measured from photographs of live embryos mounted dorsally, and normalised for the size of the head, using CELLB software (for details, see Fig. 7—Supplemental file 2).

An LD50 curve was plotted for the adjusted exposure time (60–110 hpf), using 16 LWT wild-type embryos (biological replicates) per concentration. To avoid cross-contamination from dead embryos, each wild-type (LWT) embryo was kept in a separate well of a 96-well plate. At the end of each treatment, the number of dead embryos (no heartbeat for 10 seconds) was recorded.

Microscopy and photography

Still images of live embryos were taken using an Olympus BX51 microscope, C3030ZOOM camera and CELLB software, and assembled with Adobe Photoshop. All micrographs are lateral views with anterior towards the left and dorsal towards the top, unless otherwise stated. For archiving, fixed and stained embryos were imaged in MultiScreen-Mesh plates containing 50% glycerol, using a Nikon AZ100 microscope with an automated stage (Prior Scientific). A compressed in-focus image was generated using the NIS-Elements Extended Depth of Focus software (Nikon).

Time-lapse imaging of live embryos was performed on a Zeiss Z.1 light-sheet microscope. *adgrg6*^{fr24} homozygous mutant embryos in a *Tg(smad6b:GFP)* background were mounted at 60 hpf in 0.7% agarose with anaesthetic (MS-222; 160 µg/ml) and 0.003% PTU (to prevent pigment formation). Images were taken of a dorsal view of the ear every 5 minutes (200 *z*-slices, 1 µm sections). A control time-lapse of a wild-type sibling embryo (images taken at 10-minute intervals) was taken on a separate day. Images were cropped and a subset of *z*-slices through the anterior (*adgrg6*^{fr24}) and posterior (phenotypically wild-type sibling) projections were used to make Maximum Intensity Projection movies of projection fusion in the wild-type sibling and the swollen projections in *adgrg6*^{fr24} mutant embryo. The two movies do not correspond exactly to the same developmental stage.

Chemoinformatics analysis and data visualisation

Chemical structures of the library compounds represented as SMILES (Weininger, 1988) were obtained from vendor catalogues. Molecules were standardised using the wash procedure of MOE (Chemical Computing Group Inc., Molecular Operating Environment

(MOE), Montréal, QC, 2011), accessed through KNIME (Berthold et al., 2009). Standardised molecules were analysed using RDKit (RDKit: Open-Source Cheminformatics, http://www.rdkit.org/, accessed 06 Nov. 2018) in Python (Python Software Foundation: Python language reference, version 3, https://www.python.org/, accessed 06 Nov. 2018). Morgan fingerprints of radius 2 (equivalent to ECFP4 (Rogers and Hahn, 2010)) were computed for each compound. Compound similarity was calculated using the Tanimoto coefficient (Willett et al., 1998) of the fingerprints using the scikit-learn library (Pedregosa et al., 2011). Based on the similarity matrix between all compound pairs, a dendrogram was obtained using the SciPy library (SciPy: Open Source Scientific Tools for Python, http://www.scipy.org/, accessed 06 Nov. 2018). The polar scatterplot was created using the matplotlib library (printed version) (Hunter, 2007) and plotly (interactive version) (Plotly Technologies Inc, Collaborative data science, Plotly, Montréal, QC, 2015.). To identify duplicated molecules, the InChIKey (Heller et al., 2015) was computed for each compound and all pairs of compounds were checked for identical InChIKeys. To create the compound network, the similarity matrix computed for the dendrogram was transformed into an adjacency matrix using a threshold value of 0.5, i.e. compounds with a similarity value over 0.5 are connected with an edge. The network visualisation was created using Cytoscape (Shannon et al., 2003).

Statistical analysis

Statistical analyses were performed using GraphPad Prism version 7 for Mac, GraphPad Software, La Jolla California USA, www.graphpad.com.

Acknowledgements

We thank a number of undergraduate and MSc project students who contributed to early stages of the primary screens described here, especially D. Butler, who helped with establishing the *mbp* secondary screening protocol. F-S. Geng tested the initial screening protocol on wild-type embryos. We thank J-P. Ashton, S. Burbridge, M. Marzo and N. van Hateren for technical support, D. Lambert for discussion and the Sheffield aquarium staff for expert care of the zebrafish.

Ethics statement

All animal work was performed under licence from the UK Home Office.

Funding

This work was funded by grants from the BBSRC (BB/J003050/1; BB/M01021X/1) to TTW and SB). ED was supported by a PhD studentship from the University of Sheffield (314420);

AA was supported by a BBSRC White Rose National Productivity Investment Fund Doctoral Training Award (BB/R50581X/1); LA was supported by a Wellcome Trust VIP award (085441). Light-sheet imaging was carried out in the Sheffield Wolfson Light Microscopy Facility, supported by a BBSRC ALERT14 award (BB/M012522/1) to TTW and SB. The Sheffield Zebrafish Screening Unit and zebrafish aquaria were supported by grants from the MRC (G0802527, G0700091). The research leading to these results has received funding from the European Union's Seventh Framework Programme (FP7/2007–2013) under Grant agreement no. 612347 to VJG.

Author contributions

Designed the study: TTW, SB

Performed the experiments SB, ED, AA, CJH, DB, LA

Wrote the manuscript: TTW, SB, ED

Analysed the data: SB, ED, TTW

Chemoinformatics analysis: AVL, VJG

Supervision: TW, SB, GW

Tables and Figures

Table 1. List of the 41 hit compounds that rescued the expression of both *vcanb* and *mbp* in *adgrg6*^{tb233c} mutants, thus representing putative Adgrg6 pathway modulators

The table includes the plate and well ID, along with known activities and the average score from nine *adgrg6*^{tb233c} embryos in the *vcanb* assay, from six *adgrg6*^{tb233c} embryos in the *mbp* assay and from three *adgrg6*^{fr24} embryos in the *fr24* assay. Grey shading indicates compounds presumed to interact with Adgrg6 receptor directly, while yellow shading indicates compounds presumed to be downstream effectors of the pathway. Abbreviations: DE, dead embryos; ND, no data; S, Spectrum; T, Tocris. *Note that cilnidipine can rescue *fr24* at 40 μM (data not shown).

839

#	Plate	Well	Compound name	Known activity	*vcanb* score	*mbp* score	*fr24* score
1	S18	C09	CARAPIN-8(9)-ENE	undetermined	0.00	8.50	9.00
2	S25	D08	3-ISOBUTYL-1-METHYLXANTHINE (IBMX)	phosphodiesterase inhibitor, non-selective adenosine receptor antagonist	2.00	8.50	9.00
3	S17	F05	DEOXYGEDUNIN	neuroprotective	2.00	8.00	9.00
4	S23	F10	DIHYDROFISSINOLIDE	undetermined	2.67	7.50	9.00
5	S04	B02	IVERMECTIN	antiparasitic	2.33	7.00	9.00
6	T01	F06	SC-10	protein kinase C activator, NMDA receptor activator	5.67	6.50	9.00
7	T01	H11	1,3-DIPROPYL-8-PHENYLXANTHINE	Selective adenosine A1 receptor antagonist	3.33	6.50	9.00
8	S17	E02	3-DEOXO-3BETA-ACETOXYDEOXYDIHYDROGEDUNIN	undetermined	0.00	6.50	9.00
9	T11	F07	CILNIDIPINE*	dihydropyridine N- and L-type Ca^{2+} channel blocker	2.00	6.50	9.00
10	S13	F03	AMIODARONE HYDROCHLORIDE	coronary vasodilator, Ca^{2+} channel blocker	5.00	6.50	9.00
11	S06	E02	HYDROCORTISONE HEMISUCCINATE	glucocorticoid	3.67	6.00	9.00
12	T01	C04	(RS)-(TETRAZOL-5-YL)GLYCINE	highly potent NMDA receptor agonist	3.00	5.00	9.00
13	S02	E05	LOMEFLOXACIN HYDROCHLORIDE	antibacterial	5.33	5.00	9.00
14	S13	E04	ETHAMIVAN	CNS & respiratory stimulant	4.67	5.00	9.00
15	T08	B04	CGS 15943	potent adenosine receptor antagonist	5.33	4.50	9.00
16	S13	E09	ASTEMIZOLE	H1 antihistamine (nonsedating)	4.67	4.50	9.00
17	T02	A09	SKF 91488 DIHYDROCHLORIDE	histamine N-methyltransferase inhibitor	3.00	4.00	9.00
18	S25	F05	11ALPHA-HYDROXYPROGESTERONE HEMISUCCINATE	glucocorticoid	2.67	4.00	9.00
19	T14	A07	EFONIDIPINE HYDROCHLORIDE MONOETHANOLATE	dihydropyridine L-type and T-type Ca^{2+} channel blocker	3.67	4.00	9.00
20	T05	C09	NIFEDIPINE	dihydropyridine L-type Ca^{2+} channel blocker	4.33	7.00	8.00
21	T05	E08	CGP 37157	antagonist of mitochondrial Na^{+}/Ca^{2+} exchange	3.67	6.50	8.00
22	S05	D03	DANAZOL	anterior pituitary suppressant, anti-estrogenic	1.00	5.00	8.00
23	S18	H09	XANTHYLETIN	undetermined	1.00	4.50	8.00
24	S18	A06	FERULIC ACID	antineoplastic, choleretic, food preservative	3.67	4.00	8.00
25	S18	F02	ALPHA-DIHYDROGEDUNOL	undetermined	2.33	4.00	8.00
26	T05	F04	(S)-(+)-NIGULDIPINE HYDROCHLORIDE	dihydropyridine L-type Ca^{2+} channel blocker, α1 antagonist	3.67	5.00	7.00
27	T07	F02	TRACAZOLATE HYDROCHLORIDE	subtype-selective $GABA_A$ allosteric modulator	2.33	4.50	7.00
28	S10	E02	NIMODIPINE	dihydropyridine L-type Ca^{2+} channel blocker	0.33	7.00	6.00
29	S17	E06	3BETA-ACETOXYDEOXODIHYDROGEDUNIN	undetermined	2.00	4.50	5.00
30	S17	F02	DIHYDROGEDUNIN	undetermined	1.67	5.00	2.00
31	S22	F09	TANGERITIN	undetermined	1.33	5.50	1.00
32	S10	F07	COLFORSIN	adenylate cyclase activator, antiglaucoma, hypotensive, vasodilator	0.00	9.00	0.00
33	T04	G02	IMILOXAN HYDROCHLORIDE	selective α_{2B}-adrenoceptor antagonist.	0.67	9.00	ND
34	S24	C03	3ALPHA-ACETOXYDIHYDRODEOXYGEDUNIN	undetermined	0.33	8.50	DE
35	S11	E02	EZETIMIBE	antihyperlipidemic (sterol absorption inhibitor)	2.00	7.50	0.00
36	S10	E06	NITRENDIPINE	dihydropyridine L-type Ca^{2+} channel blocker	1.33	7.00	ND
37	S11	E08	ROSUVASTATIN CALCIUM	antihyperlipidemic	0.00	6.00	0.00
38	S22	C07	DEMETHYLNOBILETIN	undetermined	0.00	6.00	0.00
39	S22	G11	HEXAMETHYLQUERCETAGETIN	undetermined	0.00	5.50	DE
40	S22	F08	NOBILETIN	matrix metaloproteinase inhibitor, antineoplastic, anti-ERK, NF-κB suppressor	0.00	5.00	DE
41	S12	H07	PREGNENOLONE SUCCINATE	glucocortcoid, antiinflammatory	4.67	4.00	DE

840

841

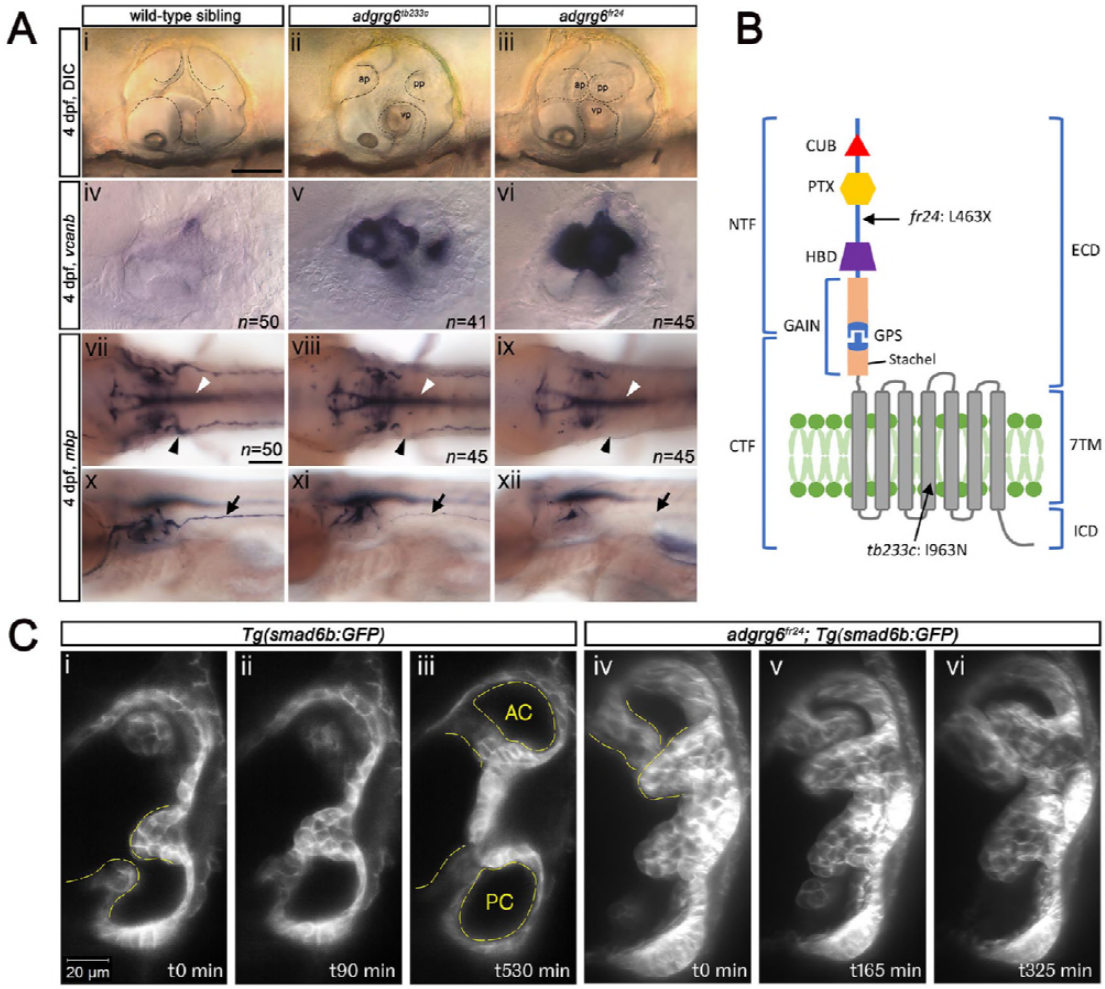

Figure 1. Comparison of *adgrg6* mutant allele phenotypes in the inner ear and peripheral nervous system

A. (i–iii) Live images of 4 dpf otic vesicles, lateral view**.** (i) wild-type sibling, (ii) *adgrg6*^{tb233c}, (iii) *adgrg6*^{fr24} showing the swollen, unfused projections in the mutant otic vesicles in ii and iii compared with the fused pillars in the wild-type ear. **(iv–vi)** ISH with *vcanb* at 4 dpf. (iv) Wild-type sibling, (v) *adgrg6*^{tb233c}, (vi) *adgrg6*^{fr24} mutant ears showing overexpression of *vcanb* in the unfused projections. Stronger staining is seen in the stronger allele, *fr24*. **(vii–xi)** ISH with *mbp* at 4dpf, (vii-ix) dorsal views, (x–xii) lateral views. (vii, x) wild-type sibling, (viii, xi) *adgrg6*^{tb233c}, (ix, xii) *adgrg6*^{fr24} showing complex staining patterns in the PNS (black arrows and arrowheads) and CNS (white arrowheads). *mbp* staining in the PLLg is absent in both *tb233c* and *fr24* alleles (black arrowheads); staining in the posterior lateral line nerve is variable in *tb233c* mutants and absent in *fr24* mutants (black arrows). **B.** Schematic diagram showing the structure of the Adgrg6 receptor and the positions of the predicted amino acid changes for the two *adgrg6* mutant alleles used in this study. **C.** Light-sheet microscope images using a *Tg(smad6b:GFP)* line, showing a dorsal view of the ear (anterior to the top). (i–iii) Wild-type sibling showing anterior and posterior pillars formed from fused projections (iii). Note that images are flipped horizontally from the originals for ease of comparison (see Supplementary Video 1; t0 on the stills corresponds to ~100 mins into the video). (iv–vi) still images from a time-lapse movie of *adgrg6*^{fr24} mutant with unfused projections that rotate around each other (see Supplementary Video 2). Abbreviations: AC, lumen of anterior semicircular canal; ap, anterior projection; CTF, carboxy-terminal fragment; CUB, Complement C1r/C1s, Uegf, BMP1 domain; ECD, extracellular domain; GAIN, GPCR auto-proteolysis domain; GPS, GPCR proteolytic site; HBD, hormone binding domain; ICD, intracellular domain; NTF, amino-terminal fragment; PC, lumen of posterior semicircular canal; pp, posterior projection; PTX, Pentraxin domain; vp, ventral projection; 7TM, 7-transmembrane domain. Scale bars: 50 µm in Ai, for Aii–vi; 100 µm in Avii, for Aviii–xii; 20 µm in Ci, for Cii–vi.

868 **Supplementary Video 1**

869 Light-sheet microscope time-lapse movie using the *Tg(smad6b:GFP)* line, which marks cell
870 membranes of the otic epithelium. Dorsal view (anterior to top) of the left inner ear of a phenotypically
871 wild-type sibling embryo showing the anterior, lateral and posterior projections (the anterior projection
872 is partially out of view). In the movie, the posterior projection grows and meets the posterior bulge
873 from the lateral projection. The projection and bulge meet, fuse and resolve to form a pillar over 900
874 minutes (approximately 55 hpf–70 hpf). The movie shows a Maximum Intensity Projection of selected
875 *z*-slices spanning approximately 6 µm, captured every 10 minutes, and played back at 10 frames per
876 second. Selected stills from the movie, flipped horizontally to match the panels showing the mutant
877 ear, are shown in Fig. 1C.

878 **Supplementary Video 2**

879 Light-sheet microscope time-lapse movie using the *Tg(smad6b:GFP)* line. Dorsal view of the right
880 inner ear of an *adgrg6*^{fr24} mutant embryo showing anterior, lateral and posterior projections (the
881 posterior projection is partially out of view). In the movie, the anterior projection and anterior bulge
882 from the lateral projection touch, but continue to grow past one another. The unfused projections
883 rotate around each other over 900 minutes (approximately 60 hpf–75 hpf). The movie shows a
884 Maximum Intensity Projection of selected *z*-slices spanning approximately 20 µm, captured every 5
885 minutes, and played back at 20 frames per second. Selected stills from the movie are shown in Fig.
886 1C.

887

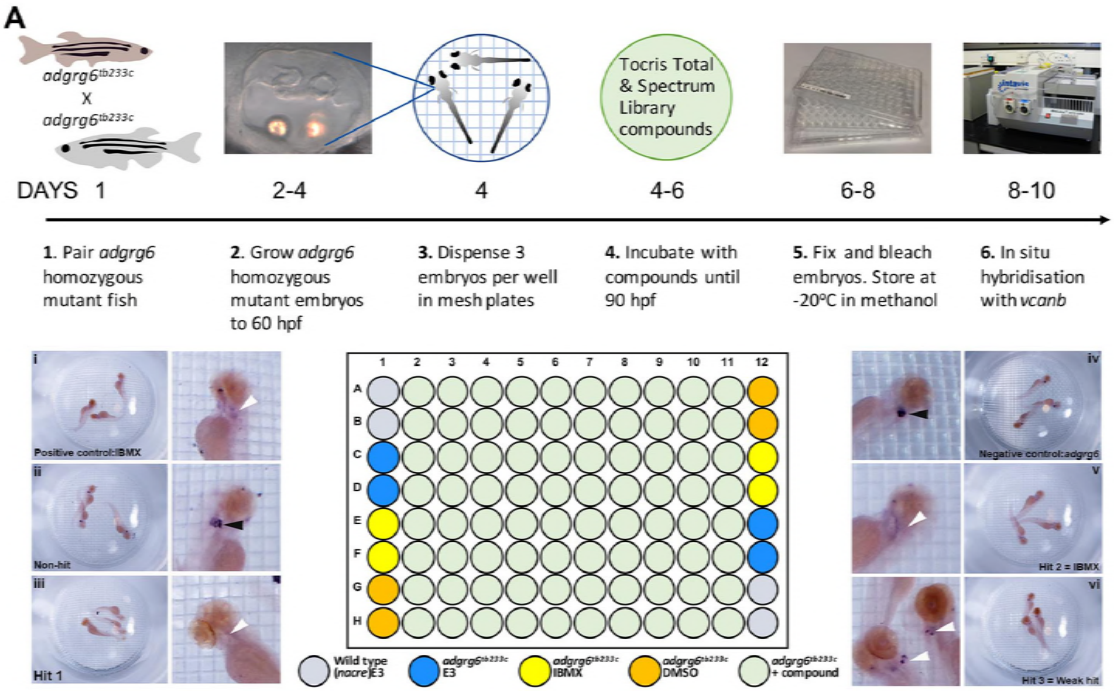

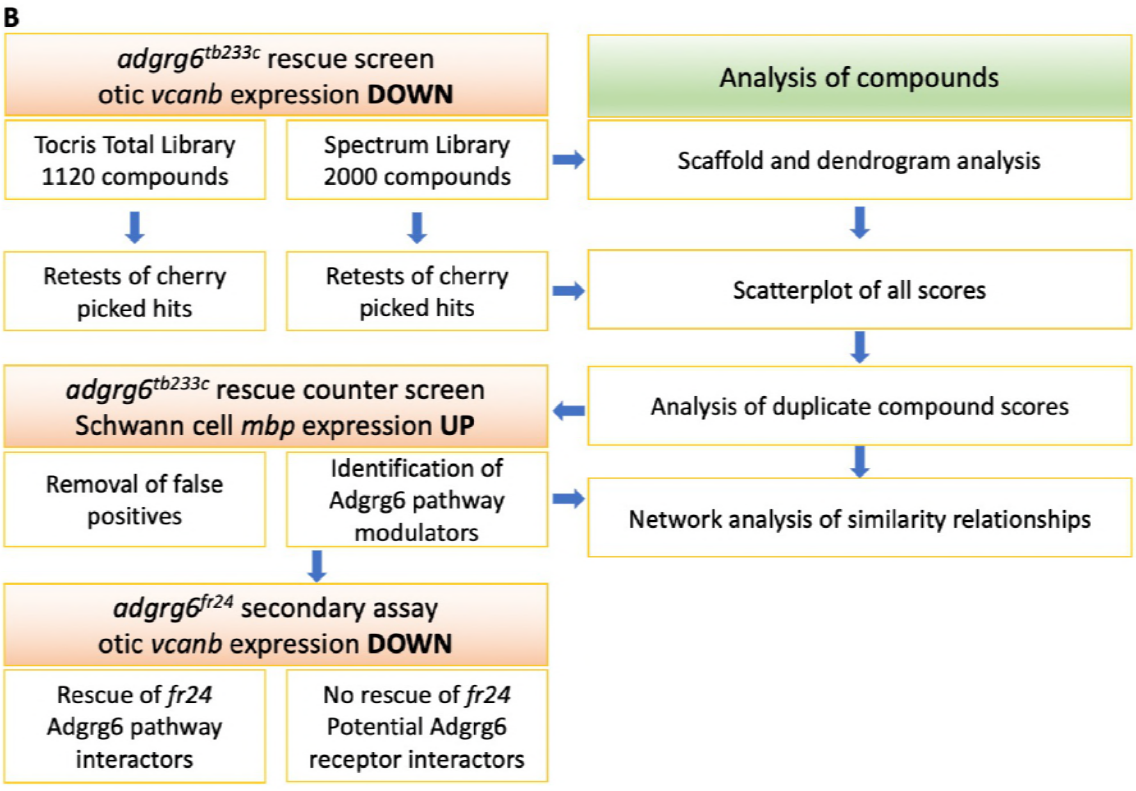

Figure 2. Overview of the screening assay protocol and strategy

A. Schematic of the screening assay protocol. Homozygous adult *adgrg6*^{tb233c} mutant fish were paired to raise large numbers of *adgrg6*^{tb233c} mutant embryos. Embryos were grown until 60 hpf, when the lateral, anterior and posterior epithelial projections in the inner ear are evident. Three embryos were aliquoted into each well of a mesh-bottomed multiwell plate in E3 medium. The mesh-

bottomed plate was then transferred to the drug plate containing control compounds as shown in the plate layout and library compounds at 25 µM in 250 µL of E3 embryo medium. Plates were incubated at 28°C until 90 hpf. The mesh-bottomed plate and embryos were then transferred to 4% PFA for fixation (4°C, overnight) and then processed for ISH to *vcanb*. Micrographs show a selection of typical results. Treatment with 100 µM IBMX (positive control, top) results in loss (rescue) of otic *vcanb* expression (white arrowhead). Strong otic *vcanb* expression (black arrowhead) is evident in embryos where the compound had no effect (non-hit) and in negative control wells (not shown). Note the spot of stain in each embryo, marking expression in the otic vesicle. Three examples are shown of wells where compounds were scored as a hit; one of these (Hit 2) was IBMX, represented in the Spectrum collection. **B**. Pipeline of the compound screening strategy and chemoinformatics analysis. The left hand side describes the flow of experimental work and the right hand side describes the complementary chemoinformatics processes. For details, see the text.

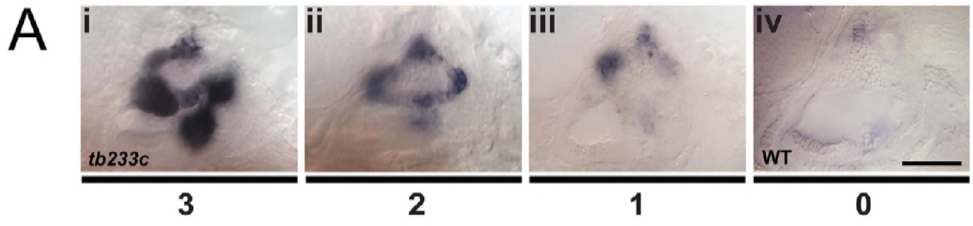

B

Category	vcanb score sum (n=3)	No. of drugs in Tocris	No. of drugs in Spectrum
A	0-2	25	68
B	>2-4	52	56
C	>4-6	15	81
D	>6-7.5	99	269
E	>7.5-9	869	1413
F	Developmental abnormality	37	68
G	No fish	23	45

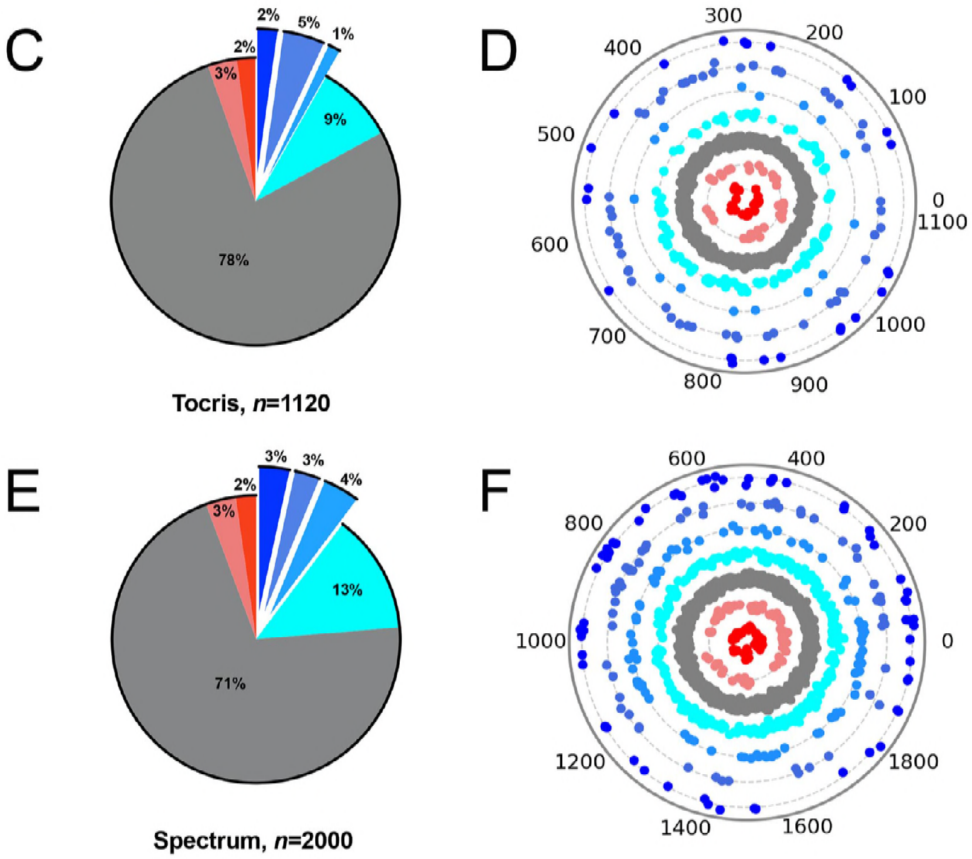

Figure 3. A primary drug screen identified 92 (Tocris) and 205 (Spectrum) putative hit compounds able to down-regulate *vcanb* mRNA expression in *adgrg6*^{tb233c} mutants

A. Scoring system used to assess *vcanb* mRNA expression levels in the inner ear of *adgd6*^{tb233c} embryos after treatment. (Ai) *vcanb* mRNA expression in the untreated/DMSO-treated *adgd6*^{tb233c} mutant ear (score 3). Scores 2 (Aii) and 1 (Aiii) were given to embryos that showed reduced *vcanb* mRNA expression to some extent, with 1 given for a stronger down-regulation than 2. (Aiv) Score 0 was given to embryos where *vcanb* mRNA levels were equivalent to wild-type levels. **B.** Compounds were categorised A–G according to the total *vcanb* score from the three embryos treated. Colours for each category correspond to the colours used in panels C–F. **C,E.** Pie charts showing the distribution of compounds from Tocris (C) and Spectrum (E) libraries in categories A–G. **D,F.** Compounds from Tocris and Spectrum libraries were ordered according to similarities in their chemical structure and presented as individual dots in polar scatterplots in D and F, respectively, with jitter (noise) introduced to improve visualisation. Spectrum library results have a higher level of clustering as expected from the scaffold analyses. Scale bar: 50 μm.

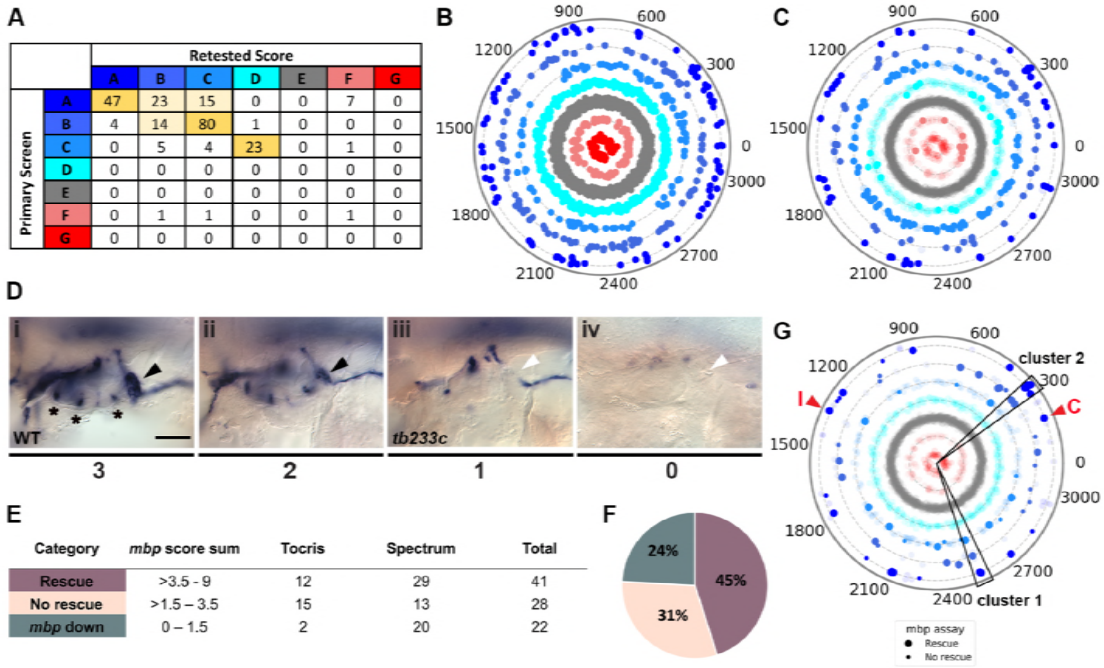

	A	B	C	D	E	F	G
A	47	23	15	0	0	7	0
B	4	14	80	1	0	0	0
C	0	5	4	23	0	1	0
D	0	0	0	0	0	0	0
E	0	0	0	0	0	0	0
F	0	1	1	0	0	1	0
G	0	0	0	0	0	0	0

Category	*mbp* score sum	Tocris	Spectrum	Total
Rescue	>3.5 - 9	12	29	41
No rescue	>1.5 – 3.5	15	13	28
mbp down	0 – 1.5	2	20	22

Figure 4. Retesting and counter screen for *mbp* expression reveals chemical clustering of hit compounds

A. Table listing the number of compounds in each scoring category after screening 9 embryos, compared to the original score after treating 3 embryos. Category thresholds and corresponding colours are the same as in Figure 3. **B**. Compounds from both libraries are represented as individual dots in the same polar scatterplot (3120 compounds in total; https://adlvdl.github.io/visualizations/polar_scatterplot_whitfield_vcanb.html). Compounds were ordered according to similarities in their chemical structure and placed in concentric circles according to the category A–G they were assigned to after the primary screen, with jitter (noise) introduced to improve visualisation. **C.** Polar scatter plot of the 91 hit compounds that passed the first retest and were followed up with *mbp* counter screens; previous scores for the compounds not followed are faded. **D–G.** *mbp* scoring system and classification of the compounds. **D.** Scoring system used to assess *mbp* mRNA expression levels in the PLLg of *adgrg6*^{tb233c} embryos after treatment. (Di) A score of 3 was given to embryos where *mbp* mRNA expression was similar to wild-type levels. Black arrowhead: *mbp* expression in PLLg; asterisks mark expression near the three cristae of the ear. (Dii) A score of 2 was given to embryos that showed *mbp* expression in the PLLg, but this was weaker than 3. (Diii) A score of 1 was given to embryos with *mbp* expression identical to the one seen in untreated *adgrg6*^{tb233c} mutants (absence of *mbp* expression in PLLg; white arrowhead). (Div) A score of 0 was used to indicate embryos where *mbp* mRNA expression was absent from the PLLg, but also reduced from the Schwann cells of the posterior and anterior lateral line. **E.** Compounds were categorised according to the *mbp* score from six embryos (average of the total score from three embryos) and grouped into compounds able to rescue *mbp* expression (score >3.5–9) and unable to rescue *mbp* expression (>1.5–3.5). A third class of compounds down-regulated both *vcanb* and *mbp* (score 0–1.5) and were not followed further. **F.** Distribution of the compounds in the different rescue categories after the *mbp* counter screen. **G.** Polar scatter plot of the final 68 hit compounds (non-faded) after *mbp* counter screens. Bigger dots represent compounds that rescued *mbp* expression, whereas smaller dots correspond to the compounds that did not rescue *mbp* expression; compounds that downregulated *mbp* expression, or were not followed, are faded. Wedges on the scatter plot delineate the two clusters of compounds with similar structures for which some hits were followed up in further analysis (see text). The positions of IBMX (I) and colforsin (C) are indicated (red arrowheads). Scale bar: 50 µm.

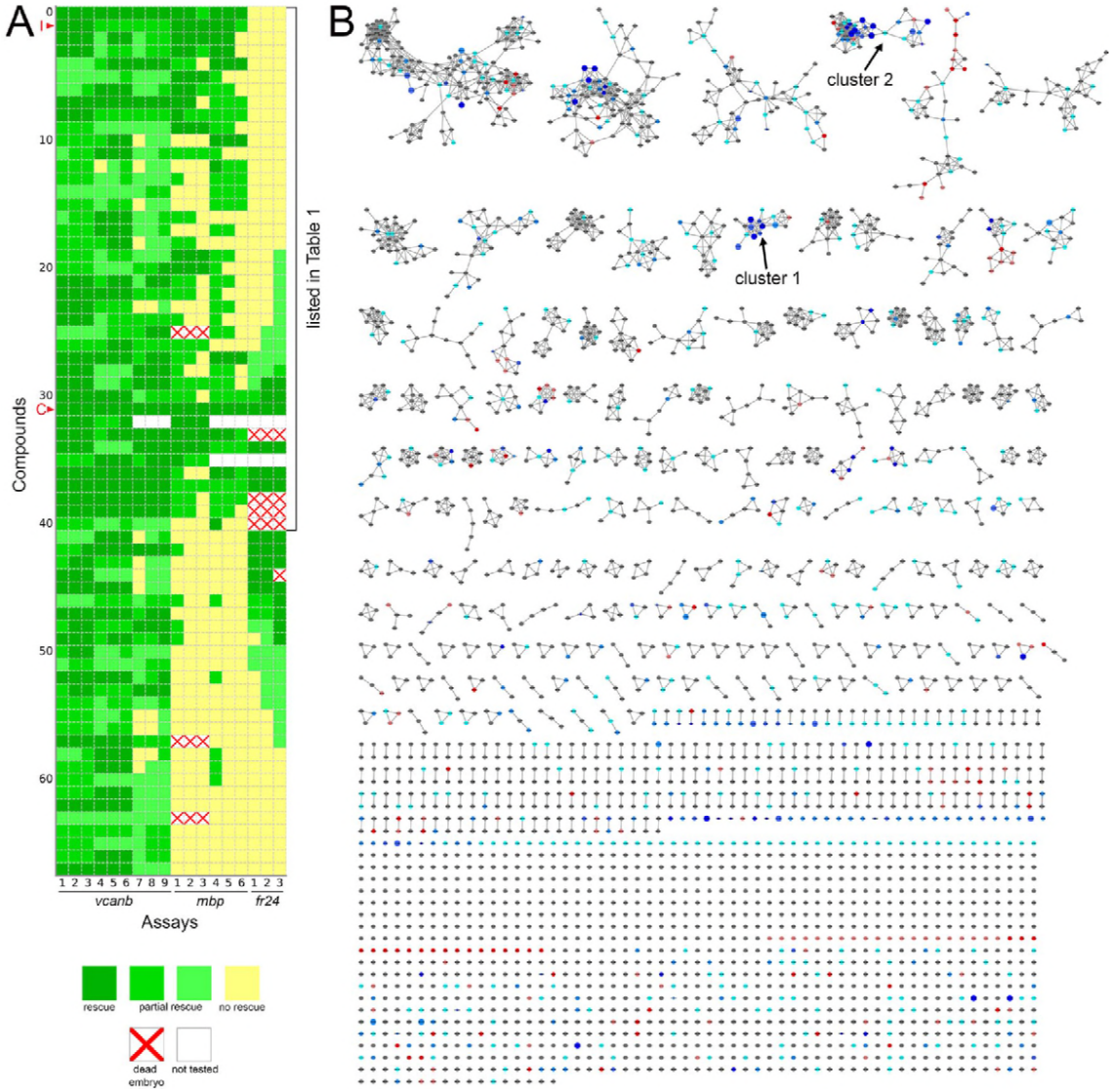

Figure 5. Heatmap of the assay results and network analysis for 68 compounds identified in *vcanb* screen

A. Heatmap of the assay results for each of the 68 hit compounds. Each box represents an embryo screened in each of the three assays (*vcanb, mbp* and *fr24*) as listed at the bottom of the heatmap. Each line corresponds to a different compound. Colours correspond to the scoring system used for each screen (0–3), with dark green, a strong hit (rescue of the mutant phenotype); yellow, no rescue; white, no data; white with red cross, toxic. Compounds were sorted based on the average score for *mbp* with strongest rescue at the top. The bracket indicates the 41 compounds that rescued both *vcanb* and *mbp* expression in *adgrg6*^{tb233c} mutants and thus represent putative Adgrg6 pathway modulators. Abbreviations: C, colforsin; I, IBMX. **B.** Network analysis based on structural similarity, showing all 3120 compounds from the two libraries. Compounds that rescued *mbp* expression are shown as larger nodes, while compounds that did not rescue *mbp* expression are shown as smaller nodes. The colours used for compounds/nodes correspond to categories A–G (as indicated in Figure 3) and the two clusters of structurally similar compounds highlighted in Figure 4 are also shown here. An interactive version of this figure can be accessed and mined at: https://adlvdl.github.io/visualizations/network_whitfield_vcanb_mbp/index.html.

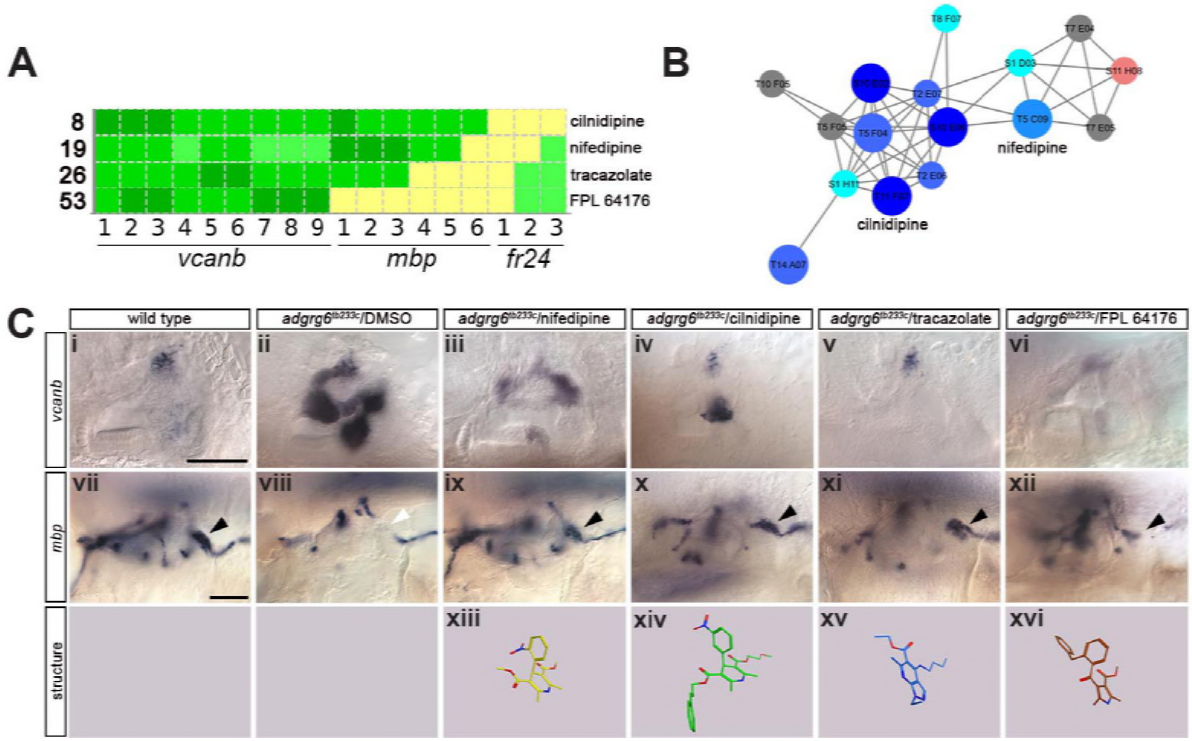

Figure 6. Hit compounds from the *vcanb* screen vary in their ability to restore *mbp* expression in *adgrg6*^{tb233c} mutant embryos

A. Section of the heatmap in Fig. 5A showing the results for two compounds from cluster 1 (cilnidipine, nifedipine), together with tracazolate hydrochloride and FPL 64176. **B.** Enlargement of the dihydropyridine cluster (cluster 1 in Figs 4G, 5B), highlighting cilnidipine and nifedipine. Compounds that rescued *mbp* expression are shown as larger nodes, while compounds that did not rescue *mbp* expression are shown as smaller nodes. **C.** (i–vi) Lateral images of the inner ear at 4 dpf stained for *vcanb* by ISH. (i) wild-type, (ii) *adgrg6*^{tb233c} mutant treated with DMSO as a control, (iii–vi) treatment of *adgrg6*^{tb233c} mutants with test compounds. Black arrowheads indicate *mbp* expression in the PLLg; white arrowhead in (viii) indicates the position of the PLLg in the untreated mutant, lacking *mbp* expression. (vii–xii) *mbp* mRNA expression of embryos listed above. Cilnidipine, nifedipine and tracazolate hydrochloride all rescued *mbp* expression in the PLLg, while FPL 64176 did not rescue *mbp* expression in the PLLg so efficiently. (xiii–xvi) 3D representation of the chemical structure of the four compounds tested. Scale bar in (i), 50 μm (applies to i-vi); scale bar in vii, 50 μm (applies to vii-xii).

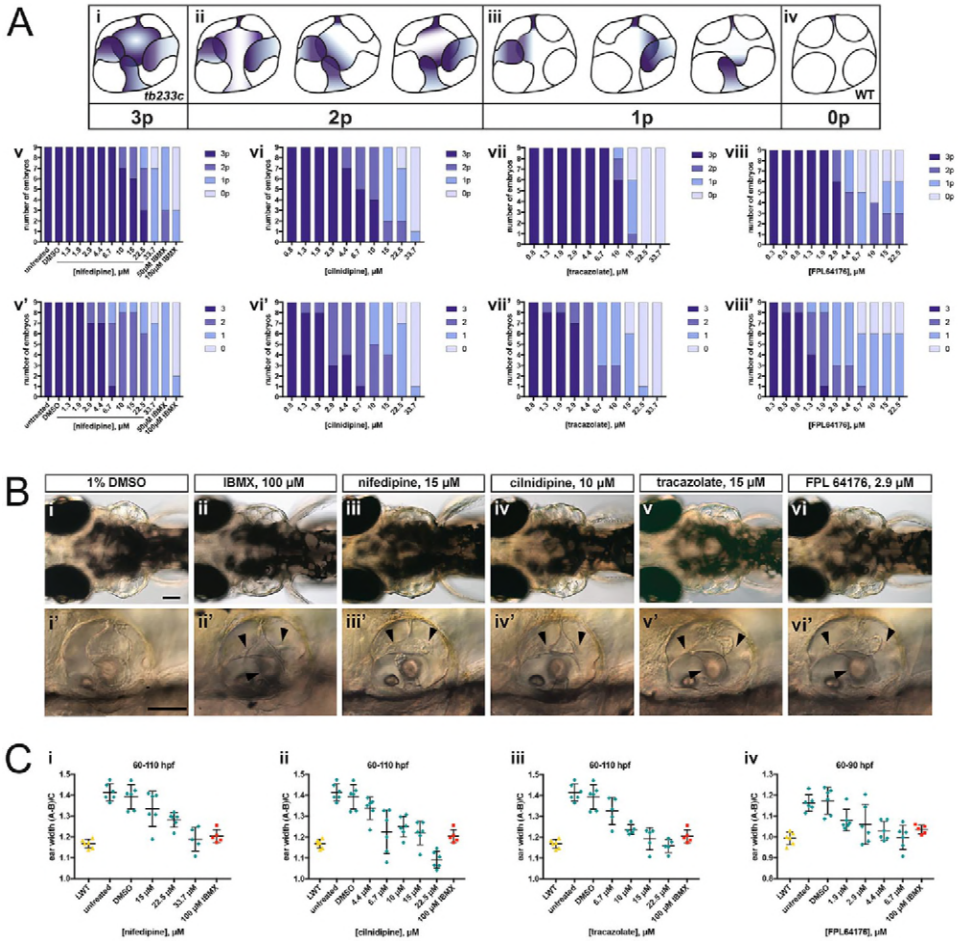

995

996 **Figure 7. Selected hit compounds rescue the *adgrg6*^{tb233c} mutant ear phenotype in a dose-**
997 **dependent manner**

998 **A.** *adgrg6*^{tb233c} homozygous embryos were exposed to a 1.5-fold dilution series of concentrations
999 (ranging from 0.3 µM to 33.7 µM), tailored to the toxicity of nifedipine, cilnidipine, tracazolate
1000 hydrochloride and FPL 64176. IBMX (50 µM and 100 µM) was used as a positive control; DMSO
1001 (1%) was used as a negative control. Embryos were treated between 60–110 hpf prior to fixation and
1002 analysis for *vcanb* expression by whole-mount in situ hydridisation. (Ai–iv) Scoring system used to
1003 assess the intensity of *vcanb* ISH staining. (Av–viii) Chart bars showing the number of embryos that
1004 scored 0p, 1p, 2p, or 3p. (Av'–viii') Chart bars showing the number of embryos that scored 0, 1, 2, or
1005 3. **B.** (i–vi) Live dorsal DIC images of 110 hpf (or 90 hpf for FPL 64176-treated embryos)
1006 *adgrg6*^{tb233c} mutants treated with the compounds shown above. (i'–vi') Lateral views of the inner ear
1007 of the embryos depicted in i–vi, showing rescue of pillar fusion (arrowheads) following treatment. **C.**
1008 Measurements of the ear-to-ear width were taken from live embryos mounted dorsally and
1009 photographed at a focal plane that highlighted the largest visible dimensions (see Fig. 7—
1010 Supplemental file 2). Error bars represent the mean ± standard deviation. Combined data from two
1011 experimental repeats. Scale bars: 50 µm.
1012

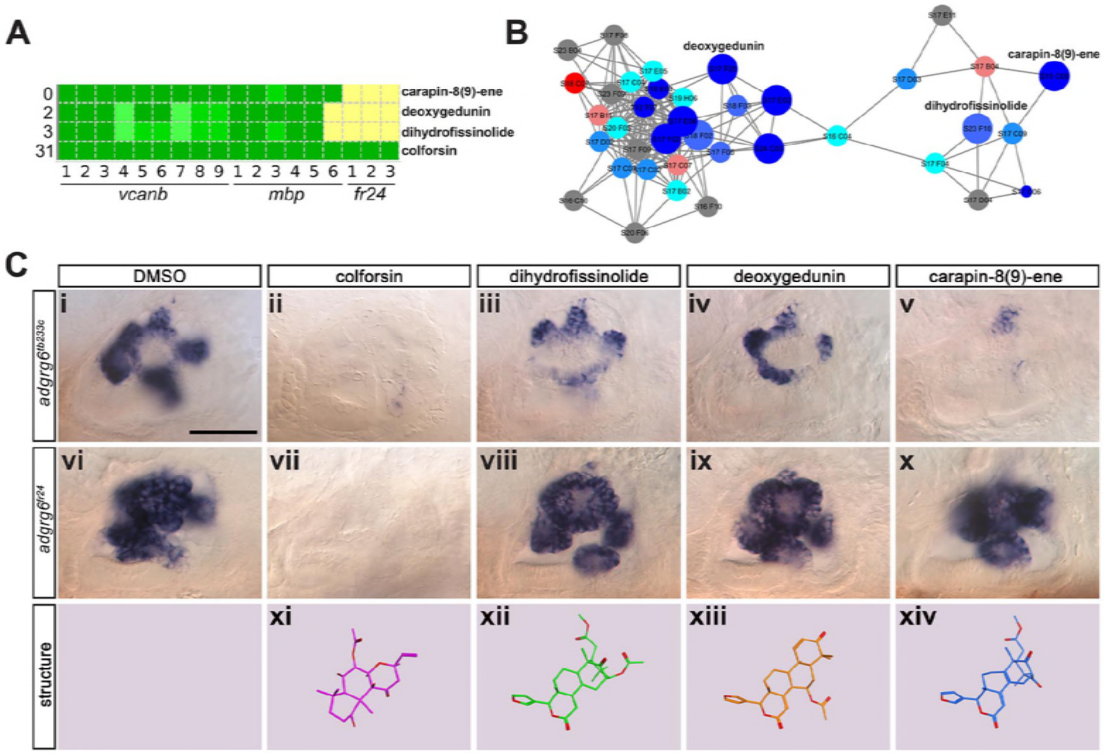

Figure 8. Assay for rescue of the *fr24* strong allele distinguishes compounds likely to rescue downstream, or at the level of, the Adgrg6 receptor

A. Section of the heatmap in Fig. 5A showing the results for colforsin, dihydrofissinolide, deoxygedunin and carapin-8(9)-ene. **B.** Enlargement of the cluster containing gedunin-related compounds (cluster 2 in Figs. 4G and 5B), highlighting deoxygedunin, dihydrofissinolide and carapin-8(9)-ene. Compounds that rescued *mbp* expression are shown as larger nodes, while compounds that did not rescue *mbp* expression are shown as smaller nodes. **C.** (i–x) Lateral images of the inner ear at 4 dpf stained for *vcanb*. (i) *adgrg6*^{tb233c}/DMSO mutant control. (ii – v) Treatment of *adgrg6*^{tb233c} mutants with compounds labelled above was able to rescue the *tb233c* mutant ear phenotype at variable degrees. (vi) *adgrg6*^{fr24}/DMSO mutant control. (vii–x) Treatment of *adgrg6*^{fr24} mutants with colforsin rescued otic *vcanb* expression in *fr24* allele, whereas treatment with dihydrofissinolide, deoxygedunin and carapin-8(9)-ene was unable to rescue the *fr24* ear phenotype. (xi–xiv) 3D representation of the chemical structure of the four compounds tested. Note the structural similarity between deoxygedunin, dihydrofissinolide and carapin-8(9)-ene. Scale bar: 50 μm.

Supplementary figures

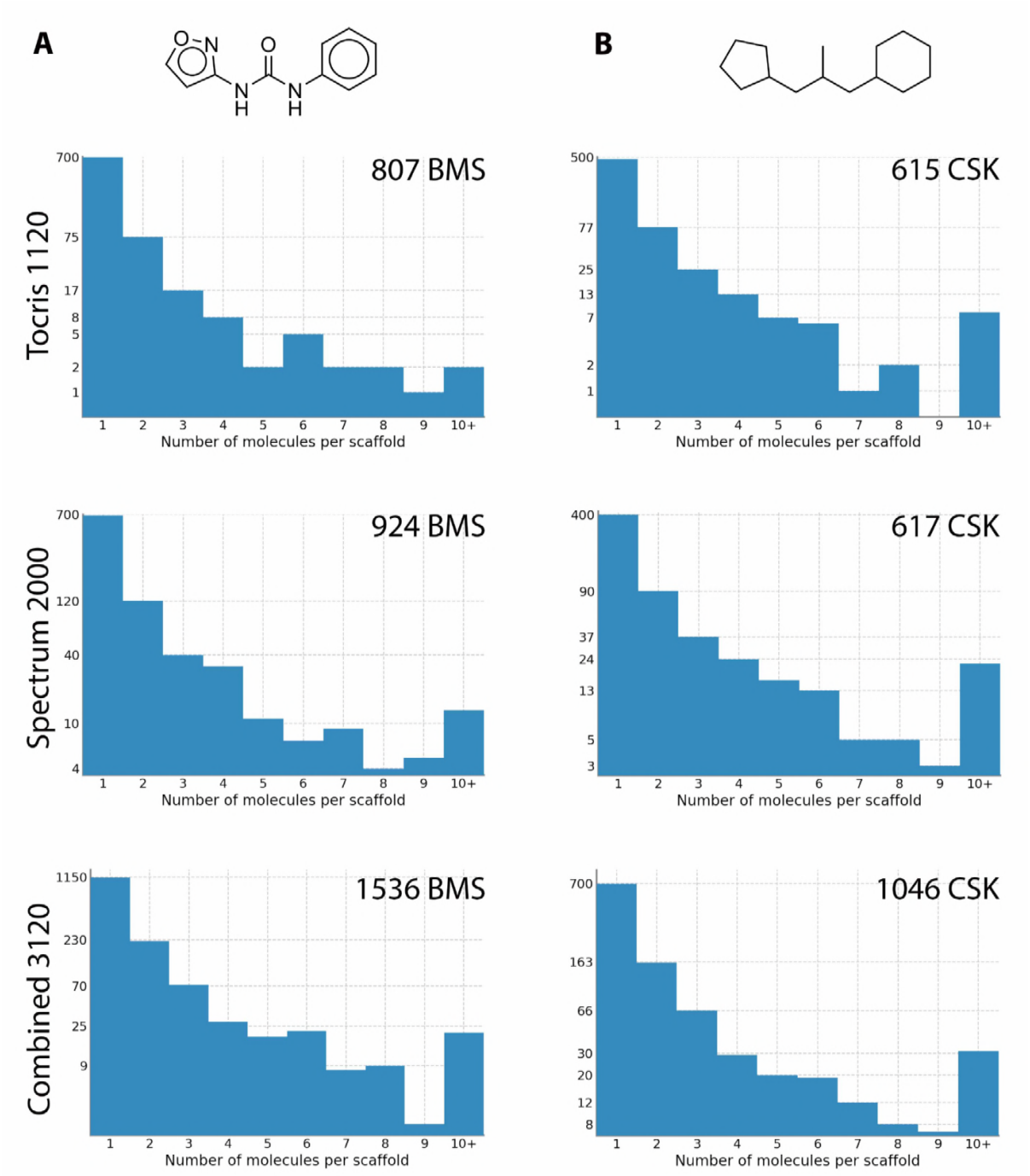

Figure 3—Supplemental file 1. Scaffold analysis of compound structures in the Tocriscreen Total and Spectrum libraries

Two different methods were used to remove side chains and determine the core structures of each compound. Scaffolds were then compared and a histogram produced with the number of molecules per scaffold. The histograms on the left use Bemis and Murcko scaffolds (Bemis and Murcko, 1996), an example of which shown at the top. The histograms on the right were generated using CSK scaffolds. The number of scaffolds for each library is shown in the top right of each graph. An exemplary BMS scaffold and CSK scaffold (obtained from the same compound) are shown above the histograms.

Figure 3—Supplemental File 2. Dendrograms representing structural similarity between library compounds

A. Dendrogram—Tocris

Dendrogram of the Tocriscreen Total library compounds based on the similarity matrix between all pairs of compounds (Ward's method of hierarchical agglomerative clustering—see Materials and Methods). Compounds are named by their plate and well ID.

B. Dendrogram—Spectrum

Dendrogram of the Spectrum library compounds based on the similarity matrix between all pairs of compounds. Compounds are named by their plate and well ID.

C. Dendrogram—Combined

Dendrogram of the combined Spectrum and Tocriscreen Total library compounds based on the similarity matrix between all pairs of compounds. Compounds are named by their plate and well ID.

Figure 4B interactive version. Scatter plot of results from the primary screen (*adgrg6*^{tb233c} *vcanb* rescue) of Tocris and Spectrum libraries combined. Hover over individual dots for compound identity. https://adlvdl.github.io/visualizations/polar_scatterplot_whitfield_vcanb.html

Figure 5B interactive version. Network analysis based on structural similarity, showing all 3120 compounds from the Tocris and Spectrum libraries. Compounds that rescued *mbp* expression are shown as larger nodes, while compounds that did not rescue *mbp* expression are shown as smaller nodes. The colours used for compounds/nodes correspond to categories A–G (as indicated in Figure 3) and the two clusters of structurally similar compounds highlighted in Figure 4 are also shown here. Zoom into individual nodes for Spectrum (S) and Tocris (T) plate number and well identity (cross-reference to Supplementary Table S1).
https://adlvdl.github.io/visualizations/network_whitfield_vcanb_mbp/index.html.

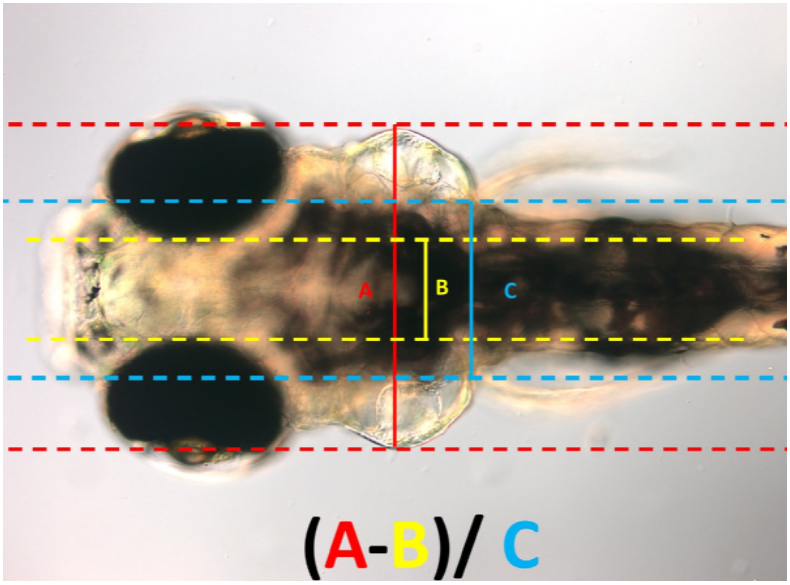

Figure 7—Supplemental file 1. Normalisation of ear width with respect to size of the head

Live DIC image of an *adgrg6*^{tb233c} mutant embryo at 110 hpf, mounted dorsally with anterior to the left, showing the parameters A, B and C (as defined in the figure) used to calculate the normalised ear width. This value was used to assess how the ear swelling is affected after treatment with different compounds.

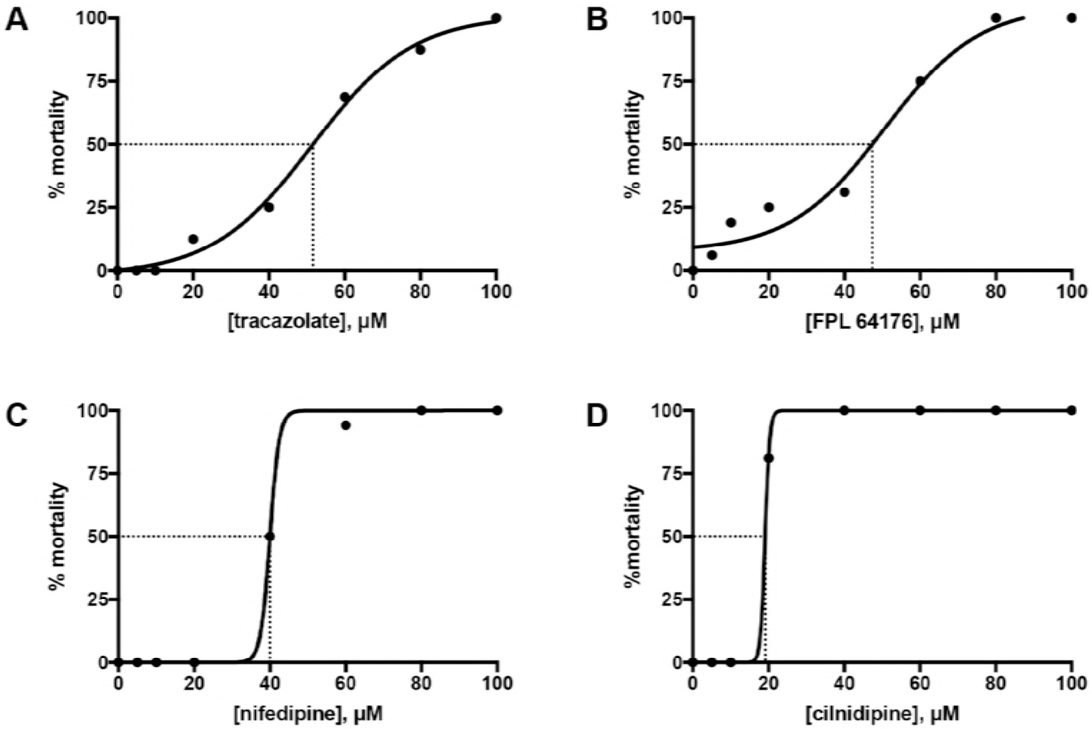

Figure 7—Supplemental file 2. LD50 curves from the treatment of wild-type embryos from 60–110 hpf

Sixteen LWT wild-type embryos, each kept in a separate well of a 96-well plate, were treated with each of the following concentrations: 5, 10, 20, 40, 60, 80 and 100 µM, from 60 to 110 hpf. At the end of the treatment, the number of alive versus dead embryos was counted and the mortality percentage was plotted against concentration. PRISM LD50, a nonlinear fit algorithm, was used to draw the curves for tracazolate hydrochloride **(A)**, FPL 64176 **(B)**, nifedipine **(C)** and cilnidipine **(D)**. The LD50 was calculated as the concentration at which 50% of the embryos were dead.

Supplementary Table S1. List of the 89 hit compounds that rescued the expression of *vcanb* in *adgrg6*^{tb233c} mutants and were followed up by *mbp* counter screens. The table includes the plate and well position of each compound, along with known activities and the raw data scores from nine *adgrg6*^{tb233c} embryos in the *vcanb* assay (v1–v9), from six *adgrg6*^{tb233c} embryos in the *mbp* assay (m1–m6) and from three *adgrg6*^{fr24} embryos in the *fr24* (fr1–3) assay. Abbreviations: DE, dead embryo; ND, no data; S, Spectrum; T, Tocris.

#	Plate	Well	Compound name	Known activity	v1	v2	v3	v4	v5	v6	v7	v8	v9	m1	m2	m3	m4	m5	m6	fr1	fr2	fr3
1	S18	C09	CARAPIN-8(9)-ENE	undetermined	0	0	0	0	0	0	0	0	0	3	3	2	3	3	3	3	3	3
2	S25	D08	3-ISOBUTYL-1-METHYLXANTHINE (IBMX)	phosphodiesterase inhibitor, non-selective adenosine receptor antagonist	0	0	0	1	1	1	1	1	1	3	3	3	3	3	2	3	3	3
3	S17	F05	DEOXYGEDUNIN	neuroprotective*	0	0	0	2	0	0	2	1	1	3	3	3	3	3	1	3	3	3
4	S23	F10	DIHYDROFISSINOLIDE	undetermined	0	0	0	2	1	1	2	1	1	3	3	2	3	3	1	3	3	3
5	S04	B02	IVERMECTIN	antiparasitic	2	2	2	1	0	0	0	0	0	2	2	1	3	3	3	3	3	3
6	T01	F06	SC-10	protein kinase C activator, NMDA receptor activator	2	2	2	2	2	1	2	2	2	3	3	3	2	1	1	3	3	3
7	T01	H11	1,3-DIPROPYL-8-PHENYLXANTHINE	Selective adenosine A1 receptor antagonist	2	2	1	0	0	0	2	2	1	3	3	2	2	2	1	3	3	3
8	S17	E02	3-DEOXO-3BETA-ACETOXYDEOXYDIHYDROGEDUNIN	undetermined	0	0	0	0	0	0	0	0	0	3	3	1	2	2	2	3	3	3
9	T11	F07	CILNIDIPINE	dihydropyridine N- and L-type Ca^{2+} channel blocker	0	0	0	1	1	1	1	1	1	3	2	2	2	2	2	3	3	3
10	S13	F03	AMIODARONE HYDROCHLORIDE	coronary vasodilator, Ca^{2+} channel blocker	1	1	1	2	2	2	2	2	2	3	3	3	2	2	0	3	3	3
11	S06	E02	HYDROCORTISONE HEMISUCCINATE	glucocorticoid	1	1	1	1	0	0	3	2	2	1	1	1	3	3	3	3	3	3
12	T01	C04	(RS)-(TETRAZOL-5-YL) GLYCINE	highly potent NMDA receptor agonist	2	1	1	0	0	0	2	2	1	2	2	2	2	1	1	3	3	3
13	S02	E05	LOMEFLOXACIN HYDROCHLORIDE	antibacterial	1	1	1	3	2	1	3	2	2	1	1	1	3	2	2	3	3	3
14	S13	E04	ETHAMIVAN	CNS & respiratory stimulant	1	1	1	2	2	1	2	2	2	2	1	1	2	2	2	3	3	3
15	T08	B04	CGS 15943	potent adenosine receptor antagonist	2	2	2	2	2	2	2	1	1	1	1	1	2	2	2	3	3	3
16	S13	E09	ASTEMIZOLE	H1 antihistamine (nonsedating)	1	1	1	2	1	1	3	2	2	1	1	1	2	2	2	3	3	3
17	T02	A09	SKF 91488 DIHYDROCHLORIDE	histamine N-methyltransferase inhibitor	2	1	1	0	0	0	2	2	1	2	2	1	1	1	1	3	3	3
18	S25	F05	11ALPHA-HYDROXYPROGESTERONE HEMISUCCINATE	glucocorticoid	1	1	1	0	0	0	2	2	1	1	1	1	2	2	1	3	3	3
19	T14	A07	EFONIDIPINE HYDROCHLORIDE MONOETHANOLATE	dihydropyridine L-type and T-type Ca^{2+} channel blocker	1	1	1	1	0	0	3	2	2	2	2	1	1	1	1	3	3	3
20	T05	C09	NIFEDIPINE	dihydropyridine L-type Ca^{2+} channel blocker	1	1	1	2	1	1	2	2	2	3	3	3	2	2	1	3	3	2

21	T05	E08	CGP 37157	antagonist of mitochondrial Na^+/Ca^{2+} exchange	1	1	1	2	2	2	1	1	0	3	3	3	2	1	1	3	3	2
22	S05	D03	DANAZOL	anterior pituitary suppressant, anti-estrogenic	0	0	0	1	0	0	2	0	0	2	2	1	2	2	1	3	3	2
23	S18	H09	XANTHYLETIN	undetermined	0	0	0	0	0	0	1	1	1	2	2	1	2	1	1	3	3	2
24	S18	A06	FERULIC ACID	antineoplastic, choleretic, food preservative	0	0	0	1	1	1	3	3	2	1	1	1	2	2	1	3	3	2
25	S18	F02	ALPHA-DIHYDROGEDUNOL	undetermined	0	0	0	2	1	1	1	1	1	2	1	1	2	1	1	3	3	2
26	T05	F04	(S)-(+)-NIGULDIPINE HYDROCHLORIDE	dihydropyridine L-type Ca^{2+} channel blocker, α1 antagonist	2	2	2	2	1	1	1	0	0	DE	DE	DE	2	2	1	3	2	2
27	T07	F02	TRACAZOLATE HYDROCHLORIDE	subtype-selective $GABA_A$ allosteric modulator	1	1	1	1	0	0	1	1	1	2	2	2	1	1	1	3	2	2
28	S10	E02	NIMODIPINE	dihydropyridine L-type Ca^{2+} channel blocker	0	0	0	0	0	0	1	0	0	2	2	1	3	3	3	2	2	2
29	S17	E06	3BETA-ACETOXYDEOXODIHYDROGEDUNIN	undetermined	0	0	0	2	2	2	0	0	0	2	1	1	2	2	1	2	2	1
30	S17	F02	DIHYDROGEDUNIN	undetermined	0	0	0	2	2	1	0	0	0	2	2	2	2	2	0	2	0	0
31	S22	F09	TANGERITIN	undetermined	0	0	0	0	0	0	2	1	1	2	2	1	2	2	2	1	0	0
32	S10	F07	COLFORSIN	adenylate cyclase activator, antiglaucoma, hypotensive, vasodilator	0	0	0	0	0	0	0	0	0	3	3	3	3	3	3	0	0	0
33	T04	G02	IMILOXAN HYDROCHLORIDE	selective α_{2B}-adrenoceptor antagonist.	0	0	0	1	1	0	ND	ND	ND	3	3	3	ND	ND	ND	ND	ND	ND
34	S24	C03	3ALPHA-ACETOXYDIHYDRODEOXYGEDUNIN	undetermined	0	0	0	1	0	0	0	0	0	3	3	3	3	3	2	DE	DE	DE
35	S11	E02	EZETIMIBE	antihyperlipidemic (sterol absorption inhibitor)	0	0	0	2	2	2	0	0	0	3	3	3	2	2	2	0	0	0
36	S10	E06	NITRENDIPINE	dihydropyridine L-type Ca^{2+} channel blocker	1	1	1	0	0	0	1	0	0	3	2	2	ND	ND	ND	ND	ND	ND
37	S11	E08	ROSUVASTATIN CALCIUM	antihyperlipidemic	0	0	0	0	0	0	0	0	0	2	1	1	3	3	2	0	0	0
38	S22	C07	DEMETHYLNOBILETIN	undetermined	0	0	0	0	0	0	0	0	0	2	2	2	2	2	2	0	0	0
39	S22	G11	HEXAMETHYLQUERCETAGETIN	undetermined	0	0	0	0	0	0	0	0	0	2	2	1	2	2	2	DE	DE	DE
40	S22	F08	NOBILETIN	matrix metaloproteinase inhibitor, antineoplastic, anti-ERK*, NF-κB suppressor*	0	0	0	0	0	0	0	0	0	2	2	1	2	2	1	DE	DE	DE
41	S12	H07	PREGNENOLONE SUCCINATE	glucocortcoid, antiinflammatory	1	1	1	2	2	1	2	2	2	1	1	1	3	1	1	DE	DE	DE
42	S05	E06	DICLOFENAC SODIUM	non steroidal, antiinflammatory	2	2	2	0	0	0	3	2	1	1	1	1	1	1	1	0	0	0
43	T09	C07	GTP 14564	class III receptor tyrosine kinase (RTK) inhibitor	1	1	0	0	0	0	0	0	0	2	1	1	1	1	0	0	0	0
44	T07	H02	D-64131	tubulin polymerisation inhibitor, antitumor in vivo	1	0	0	1	1	1	3	2	2	1	1	0	1	1	1	0	0	0

45	S10	G05	IOPANIC ACID	radioopaque agent	0	0	0	2	2	2	3	2	2	1	1	0	1	1	1	0	0	DE
46	S18	H11	ANGOLENSIN (R)	antimalarial*	0	0	0	0	0	0	3	2	2	1	1	1	1	0	0	0	0	0
47	S22	G09	SINENSETIN	increases cAMP levels in adipocytes*	2	2	2	1	1	1	2	1	1	2	0	0	2	1	1	1	1	0
48	T09	F06	CMPD-1	selective inhibitor of p38α-mediated MK2a phosphorylation	0	0	0	0	0	0	1	0	0	1	1	1	1	1	0	1	1	0
49	T06	A07	BHQ	inhibitor of endoplasmic reticulum Ca^{2+}-ATPase.	1	0	0	1	1	1	0	0	0	2	1	1	1	1	1	2	2	0
50	S18	G06	2,3-DIHYDROXY-4-METHOXY-4'-ETHOXYBENZOPHENONE	undetermined	0	0	0	1	0	0	1	1	0	2	1	1	1	1	1	3	2	0
51	T06	G04	PP 1	selective Src family tyrosine kinase inhibitor	1	0	0	2	2	1	2	2	2	1	1	1	1	1	1	2	2	2
52	T12	A08	CPT 11	DNA topoisomerase I inhibitor, antitumor	2	1	1	2	2	2	2	1	1	1	1	1	1	1	1	2	2	2
53	S16	G11	MEPIROXOL	antihyperlipemic	0	0	0	0	0	0	2	1	0	1	1	1	2	1	1	3	2	2
54	T06	G10	FPL 64176	potent activator of L-type Ca^{2+} channels, N-type Ca^{2+} channel blocker	1	0	0	1	1	1	0	0	0	1	1	1	1	1	1	3	2	2
55	T08	D11	2-METHOXYESTRADIOL	apoptotic, antiangiogenic	1	1	1	2	1	1	2	2	1	1	1	1	1	1	0	3	2	2
56	S15	E10	CARBIMAZOLE	antithyroid	1	1	1	2	2	1	3	3	2	1	1	1	1	1	1	3	3	2
57	T07	D03	CGP 7930	positive modulator at $GABA_B$ receptors	1	1	1	2	1	1	3	3	2	1	1	1	1	1	1	3	3	2
58	T02	D07	METHIOTHEPIN MALEATE	potent 5-HT_2 and 5-HT_1 antagonist	0	0	0	0	0	0	1	1	1	DE	DE	DE	1	1	1	3	3	2
59	T02	A11	GBR 12935 DIHYDROCHLORIDE	selective inhibitor of dopamine uptake	2	2	1	0	0	0	3	3	1	1	1	1	2	1	1	3	3	3
60	S25	A06	CHOLIC ACID	undetermined	1	1	1	0	0	0	3	2	2	1	1	1	2	1	1	3	3	3
61	S16	F04	MANNITOL	diuretic, sweetener, diagnostic aid	1	1	1	2	2	2	2	2	2	1	1	1	2	1	1	3	3	3
62	S11	H04	DECOQUINATE	coccidiostat	1	1	1	0	0	0	2	2	2	1	1	1	1	1	1	3	3	3
63	S17	C06	3-DEOXO-3BETA-HYDROXYMEXICANOLIDE 16-ENOL ETHER	undetermined	0	0	0	0	0	0	2	2	2	1	1	1	1	1	1	3	3	3
64	T05	H11	DL-TBOA	non-transportable blocker of excitatory amino acid transporters	2	2	2	2	2	2	2	2	2	DE	DE	DE	1	1	1	3	3	3
65	T12	D09	SD 208	potent ATP-competitive TGF-βRI inhibitor	1	1	1	1	1	1	2	1	1	1	1	1	1	1	1	3	3	3
66	S18	C08	HARMINE	antiparkinsonian, CNS stimulant	1	1	1	2	2	2	2	1	1	1	1	1	1	1	1	3	3	3
67	S18	D03	7-DESHYDROXYPYROGALLIN-4-CARBOXYLIC ACID	undetermined	1	1	1	0	0	0	2	1	1	1	1	1	1	1	1	3	3	3
68	T07	C09	TMS	cytochrome P450 1B1 inhibitor	0	0	0	0	0	0	2	2	2	1	1	0	1	1	1	3	3	3

69	S19	F06	LARIXOL ACETATE	potent TRPC6 Inhibitor*	0	0	0	1	1	2	3	3	3	0	0	0	0	0	1	3	3	3
70	S02	C03	ECONAZOLE NITRATE	antifungal	0	0	0	0	0	0	2	2	2	0	0	0	0	0	0	0	0	1
71	S01	H03	MEBENDAZOLE	anthelmintic	1	1	1	0	0	0	1	1	1	0	0	1	0	0	0	0	0	0
72	S21	C06	GITOXIN	cardiotonic	1	1	1	0	0	1	0	0	0	0	0	0	0	1	1	0	0	DE
73	S19	C09	DEOXYSAPPANONE B 7,3'-DIMETHYL ETHER ACETATE	undetermined	0	0	0	0	0	0	0	0	0	0	1	1	0	0	0	2	1	0
74	S05	F04	DIGITOXIN	inotropic, cardiotonic	0	0	0	1	2	1	0	0	0	0	0	0	0	0	0	0	0	0
75	S05	G06	DISULFIRAM	alcohol antagonist	0	0	0	0	0	0	1	1	1	0	0	0	0	0	0	0	0	1
76	S02	A10	SULCONAZOLE NITRATE	antifungal	0	0	0	0	0	0	1	1	2	0	0	0	0	0	0	DE	DE	DE
77	S18	B08	BAICALEIN	antiviral (HIV)	0	0	0	0	0	0	0	0	0	1	1	1	0	0	0	0	0	DE
78	S05	B07	CLOTRIMAZOLE	antifungal	0	0	0	0	0	0	0	0	0	1	1	1	0	0	0	0	0	0
79	S03	B10	LOVASTATIN	antihyperlipidemic, HMGCoA reductase inhibitor	0	0	0	0	0	0	0	0	0	0	0	0	1	1	1	DE	DE	DE
80	S13	C11	CYPROHEPTADINE HYDROCHLORIDE	H1-antihistamine, antipruritic	0	0	0	0	0	0	0	0	0	0	0	0	0	1	1	0	0	0
81	S24	E10	5-FLUOROINDOLE-2-CARBOXYLIC ACID	NMDA receptor antagonist (gly)	0	0	0	0	0	0	0	0	0	0	0	0	1	0	0	0	0	0
82	S10	F11	ALBENDAZOLE	anthelmintic	0	0	0	0	0	0	0	0	0	0	0	0	0	0	1	0	0	0
83	S19	A05	DEOXYSAPPANONE B 7,4'-DIMETHYL ETHER	undetermined	0	0	0	0	0	0	0	0	0	1	0	0	0	0	0	0	0	0
84	S25	A03	ARTENIMOL	antimalarial, antiinflammatory	0	0	0	0	0	0	0	0	0	0	0	0	0	0	0	0	0	0
85	S16	H09	CHAULMOOGRIC ACID	antibacterial (mycobacteria)	0	0	0	0	0	0	0	0	0	0	0	0	0	0	0	0	0	0
86	S01	G06	FENBENDAZOLE	anthelmintic	0	0	0	0	0	0	0	0	0	0	0	0	0	0	0	0	0	0
87	S18	E08	GEDUNIN	antifeedant, heat shock inducer, Hsp90 inhibitor*, anticancer*	0	0	0	0	0	0	0	0	0	0	0	0	0	0	0	DE	DE	DE
88	S03	G11	PODOFILOX	antineoplastic, antimitotic	0	0	0	0	0	0	0	0	0	0	0	0	0	0	0	0	0	0
89	T07	H03	LONIDAMINE	anticancer, mitochondrial hexokinase inhibitor	0	0	0	0	0	0	ND	ND	ND	0	0	0	ND	ND	ND	ND	ND	ND

*Deoxygedunin: (Jang et al., 2010); Nobiletin: (Cheng et al., 2016); Angolensin (R): (Weisman et al., 2006); Sinensetin: (Kang et al., 2015); Larixol acetate: (Urban et al., 2016); Gedunin: (Hieronymus et al., 2006; Subramani et al., 2017).

References

Ackerman, S. D., Garcia, C., Piao, X., Gutmann, D. H. and Monk, K. R. (2015). The adhesion GPCR Gpr56 regulates oligodendrocyte development via interactions with Galpha12/13 and RhoA. *Nat Commun* **6**, 6122.

Ackerman, S. D., Luo, R., Poitelon, Y., Mogha, A., Harty, B. L., D'Rozario, M., Sanchez, N. E., Lakkaraju, A. K. K., Gamble, P., Li, J., et al. (2018). GPR56/ADGRG1 regulates development and maintenance of peripheral myelin. *J Exp Med* **215**, 941-961.

Altmann, S., Davis, H. J., Zhu, L., Yao, X., Hoos, L., Tetzloff, G., Iyer, S., Maguire, M., Golovko, A., Zeng, M., et al. (2004). Niemann-Pick C1 Like 1 protein is critical for intestinal cholesterol absorption. *Science* **303**, 1201-1204.

Andersson-Sjöland, A., Hallgren, O., Rolandsson, S., Weitoft, M., Tykesson, E., Larsson-Callerfelt, A. K., Rydell-Törmänen, K., Bjermer, L., Malmström, A., Karlsson, J. C., et al. (2015). Versican in inflammation and tissue remodeling: the impact on lung disorders. *Glycobiology* **25**, 243-251.

Baxendale, S., Holdsworth, C., Meza Santoscoy, P., Harrison, M., Fox, J., Parkin, C., Ingham, P. and Cunliffe, V. (2012). Identification of compounds with anti-convulsant properties in a zebrafish model of epileptic seizures. *Dis. Mod. Mech.* **5**, 773-784.

Baxendale, S., van Eeden, F. and Wilkinson, R. (2017). The Power of Zebrafish in Personalised Medicine. *Adv. Exp. Med. Biol.* **1007**, 179-197.

Baxendale, S. and Whitfield, T. (2016). Methods to study the development, anatomy, and function of the zebrafish inner ear across the life course. *Meth. Cell. Biol.* **134**, 165-209.

Bemis, G. and Murcko, M. (1996). The properties of known drugs. 1. Molecular frameworks. *J. Med. Chem.* **39**, 2887-2893.

Berthold, M., Cebron, N., Dill, F., Gabriel, T., Kotter, T., Meinl, T., Ohl, P., Thiel, K. and Wiswedel, B. (2009). KNIME – The Konstanz Information Miner. *SIGKDD Explorations* **11**, 26-31.

Brady, C., Rennekamp, A. and Peterson, R. (2016). Chemical Screening in Zebrafish. *Methods Mol. Biol.* **1451**, 3-16.

Braidy, N., Behzad, S., Habtemariam, S., Ahmed, T., Daglia, M., Nabavi, S. M., Sobarzo-Sanchez, E. and Nabavi, S. F. (2017). Neuroprotective Effects of Citrus Fruit-Derived Flavonoids, Nobiletin and Tangeretin in Alzheimer's and Parkinson's Disease. *CNS Neurol Disord Drug Targets* **16**, 387-397.

Brösamle, C. and Halpern, M. E. (2002). Characterization of myelination in the developing zebrafish. *Glia* **39**, 47-57.

Bruni, G., Rennekamp, A., Velenich, A., McCarroll, M., Gendelev, L., Fertsch, E., Taylor, J., Lakhani, P., Lensen, D., Evron, T., et al. (2016). Zebrafish behavioral profiling identifies multitarget antipsychotic-like compounds. *Nat. Chem. Biol.* **12**.

Buck, L. M. J., Winter, M. J., Redfern, W. S. and Whitfield, T. T. (2012). Ototoxin-induced cellular damage in neuromasts disrupts lateral line function in larval zebrafish. *Hear. Res.* **284**, 67-81.

Buckley, C., Marguerie, A., Roach, A., Goldsmith, P., Fleming, A., Alderton, W. and Franklin, R. (2010). Drug reprofiling using zebrafish identifies novel compounds with potential pro-myelination effects. *Neuropharmacology* **59**, 149-159.

Cheng, H. L., Hsieh, M. J., Yang, J. S., Lin, C. W., Lue, K. H., Lu, K. H. and Yang, S. F. (2016). Nobiletin inhibits human osteosarcoma cells metastasis by blocking ERK and JNK-mediated MMPs expression. *Oncotarget* **7**, 35208-35223.

Chowdhury, R., Candela-Lena, J., Chan, M., Greenald, D., Yeoh, K., Tian, Y., McDonough, M., Tumber, A., Rose, N., Conejo-Garcia, A., et al. (2013). Selective small molecule probes for the hypoxia inducible factor (HIF) prolyl hydroxylases. *ACS Chem. Biol.* **8**, 1488-1496.

Demberg, L., Winkler, J., Wilde, C., Simon, K., Schön, J., Rothemund, S., Schöneberg, T., Prömel, S. and Liebscher, I. (2017). Activation of Adhesion G Protein-coupled Receptors: AGONIST SPECIFICITY OF STACHEL SEQUENCE-DERIVED PEPTIDES. *J. Biol. Chem.* **292**, 4383-4394.

Early, J., Cole, K., Williamson, J., Swire, M., Kamadurai, H., Muskavitch, M. and Lyons, D. (2018). An automated high-resolution in vivo screen in zebrafish to identify chemical regulators of myelination. *Elife* **7**, e35136.

English, A. W., Liu, K., Nicolini, J. M., Mulligan, A. M. and Ye, K. (2013). Small-molecule trkB agonists promote axon regeneration in cut peripheral nerves. *Proc Natl Acad Sci U S A* **110**, 16217-16222.

Geng, F., Abbas, L., Baxendale, S., Holdsworth, C., Swanson, A. G., Slanchev, K., Hammerschmidt, M., Topczewski, J. and Whitfield, T. (2013). Semicircular canal morphogenesis in the zebrafish inner ear requires the function of *gpr126* (*lauscher*), an adhesion G protein-coupled receptor gene. *Development* **140**, 4362-4374.

Giera, S., Deng, Y., Luo, R., Ackerman, S. D., Mogha, A., Monk, K. R., Ying, Y., Jeong, S. J., Makinodan, M., Bialas, A. R., et al. (2015). The adhesion G protein-coupled receptor GPR56 is a cell-autonomous regulator of oligodendrocyte development. *Nat Commun* **6**, 6121.

Glenn, T. D. and Talbot, W. S. (2013). Analysis of Gpr126 function defines distinct mechanisms controlling the initiation and maturation of myelin. *Development* **140**, 3167-3175.

Griffin, A., Hamling, K., Knupp, K., Hong, S., Lee, L. and Baraban, S. (2017). Clemizole and modulators of serotonin signalling suppress seizures in Dravet syndrome. *Brain* **140**, 669-683.

Hamann, J., Aust, G., Arac, D., Engel, F. B., Formstone, C., Fredriksson, R., Hall, R. A., Harty, B. L., Kirchhoff, C., Knapp, B., et al. (2015). International Union of Basic and Clinical Pharmacology. XCIV. Adhesion G protein-coupled receptors. *Pharmacol Rev* **67**, 338-367.

Hauser, A., Attwood, M., Rask-Andersen, M., Schiöth, H. and Gloriam, D. (2017). Trends in GPCR drug discovery: new agents, targets and indications. *Nat. Rev. Drug Discov.* **16**, 829-842.

Heller, S., McNaught, A., Pletnev, I., Stein, S. and Tchekhovskoi, D. (2015). InChI, the IUPAC International Chemical Identifier. *J. Cheminformatics* **7**, 23.

Hieronymus, H., Lamb, J., Ross, K., Peng, X., Clement, C., Rodina, A., Nieto, M., Du, J., Stegmaier, K., Raj, S., et al. (2006). Gene expression signature-based chemical genomic prediction identifies a novel class of HSP90 pathway modulators. *Cancer Cell* **10**, 321-330.

Hruscha, A., Krawitz, P., Rechenberg, A., Heinrich, V., Hecht, J., Haass, C. and Schmid, B. (2013). Efficient CRISPR/Cas9 genome editing with low off-target effects in zebrafish. *Development* **140**, 4982-4987.

Huang, P., Zheng, S., Wierbowski, B., Kim, Y., Nedelcu, D., Aravena, L., Liu, J., Kruse, A. and Salic, A. (2018). Structural Basis of Smoothened Activation in Hedgehog Signaling. *Cell* **174**, 312-324.

Hunter, J. (2007). Matplotlib: A 2D Graphics Environment. *Comp. Sci. Engi.* **9**, 90-95.

Hwang, W., Fu, Y., Reyon, D., Maeder, M., Tsai, S., Sander, J., Peterson, R., Yeh, J. and Joung, J. (2013). Efficient genome editing in zebrafish using a CRISPR-Cas system. *Nat. Biotech.* **31**, 227-229.

Istvan, E. and Deisenhofer, J. (2001). Structural mechanism for statin inhibition of HMG-CoA reductase. *Science* **292**, 1160-1164.

Jang, S., Liu, X., Chan, C., France, S., Sayeed, I., Tang, W., Lin, X., Xiao, G., Andero, R., Chang, Q., et al. (2010). Deoxygedunin, a natural product with potent neurotrophic activity in mice. *PLoS One* **5**, e11528.

Kalueff, A. V., Echevarria, D. J., Homechaudhuri, S., Stewart, A. M., Collier, A. D., Kaluyeva, A. A., Li, S., Liu, Y., Chen, P., Wang, J., et al. (2016). Zebrafish neurobehavioral phenomics for aquatic neuropharmacology and toxicology research. *Aquat Toxicol* **170**, 297-309.

Kang, J. S., Oohashi, T., Kawakami, Y., Bekku, Y., Izpisúa Belmonte, J. C. and Ninomiya, Y. (2004). Characterization of *dermacan*, a novel zebrafish lectican gene, expressed in dermal bones. *Mech. Dev.* **121**, 301-312.

Kang, S., Shin, H. and Kim, S. (2015). Sinensetin enhances adipogenesis and lipolysis by increasing cyclic adenosine monophosphate levels in 3T3-L1 adipocytes. *Biol. Pharm. Bull.* **38**, 552-558.

Karner, C., Long, F., Solnica-Krezel, L., Monk, K. and Gray, R. (2015). Gpr126/Adgrg6 deletion in cartilage models idiopathic scoliosis and pectus excavatum in mice. *Hum. Mol. Genet.* **24**, 4365-4373.

Keough, M. B., Rogers, J. A., Zhang, P., Jensen, S. K., Stephenson, E. L., Chen, T., Hurlbert, M. G., Lau, L. W., Rawji, K. S., Plemel, J. R., et al. (2016). An inhibitor of chondroitin sulfate proteoglycan synthesis promotes central nervous system remyelination. *Nat Commun* **7**, 11312.

Komor, A., Kim, Y., Packer, M., Zuris, J. and Liu, D. (2016). Programmable editing of a target base in genomic DNA without double-stranded DNA cleavage. *Nature* **533**, 420-424.

Langenhan, T., Piao, X. and Monk, K. (2016). Adhesion G protein-coupled receptors in nervous system development and disease. *Nat. Rev. Neurosci.* **17**, 550-561.

Liebscher, I., Schön, J., Petersen, S., Fischer, L., Auerbach, N., Demberg, L., Mogha, A., Cöster, M., Simon, K., Rothemund, S., et al. (2014). A tethered agonist within the ectodomain activates the adhesion G protein-coupled receptors GPR126 and GPR133. *Cell Rep.* **9**, 2018-2026.

Lister, J. A., Robertson, C. P., Lepage, T., Johnson, S. L. and Raible, D. W. (1999). *nacre* encodes a zebrafish microphthalmia-related protein that regulates neural-crest-derived pigment cell fate. *Development* **126**, 3757-3767.

Liu, L., Gonzalez, P. K., Barrett, C. F. and Rittenhouse, A. R. (2003). The calcium channel ligand FPL 64176 enhances L-type but inhibits N-type neuronal calcium currents. *Neuropharmacology* **45**, 281-292.

Luchetti, G., Sircar, R., Kong, J., Nachtergaele, S., Sagner, A., Byrne, E., Covey, D., Siebold, C. and Rohatg, i. R. (2018). Cholesterol activates the G-protein coupled receptor Smoothened to promote Hedgehog signaling. *Elife* **5**, e20304.

Ma, W., Feng, S., Yao, X., Yuan, Z., Liu, L. and Xie, Y. (2015). Nobiletin enhances the efficacy of chemotherapeutic agents in ABCB1 overexpression cancer cells. *Sci Rep* **5**, 18789.

Millar, M. W., Corson, N. and Xu, L. (2018). The Adhesion G-Protein-Coupled Receptor, GPR56/ADGRG1, Inhibits Cell-Extracellular Matrix Signaling to Prevent Metastatic Melanoma Growth. *Front Oncol* **8**, 8.

Mogha, A., Benesh, A., Patra, C., Engel, F., Schöneberg, T., Liebscher, I. and Monk, K. (2013). Gpr126 functions in Schwann cells to control differentiation and myelination via G-protein activation. *J. Neurosci.* **33**, 17976-17985.

Monk, K. R., Hamann, J., Langenhan, T., Nijmeijer, S., Schoneberg, T. and Liebscher, I. (2015). Adhesion G Protein-Coupled Receptors: From In Vitro Pharmacology to In Vivo Mechanisms. *Mol Pharmacol* **88**, 617-623.

Monk, K. R., Naylor, S. G., Glenn, T. D., Mercurio, S., Perlin, J. R., Dominguez, C., Moens, C. B. and Talbot, W. S. (2009). A G protein-coupled receptor is essential for Schwann cells to initiate myelination. *Science* **325**, 1402-1405.

Monk, K. R., Oshima, K., Jörs, S., Heller, S. and Talbot, W. S. (2011). Gpr126 is essential for peripheral nerve development and myelination in mammals. *Development* **138**, 2673-2680.

Nie, S., Xu, Y., Chen, G., Ma, K., Han, C., Guo, Z., Zhang, Z., Ye, K. and Cao, X. (2015). Small molecule TrkB agonist deoxygedunin protects nigrostriatal dopaminergic neurons from 6-OHDA and MPTP induced neurotoxicity in rodents. *Neuropharmacology* **99**, 448-458.

North, T., Goessling, W., Walkley, C., Lengerke, C., Kopani, K., Lord, A., Weber, G., Bowman, T., Jang, I., Grosser, T., et al. (2007). Prostaglandin E2 regulates vertebrate haematopoietic stem cell homeostasis. *Nature* **447**, 1007-1011.

Owens, K. N., Santos, F., Roberts, B., Linbo, T., Coffin, A. B., Knisely, A. J., Simon, J. A., Rubel, E. W. and Raible, D. W. (2008). Identification of genetic and chemical modulators of zebrafish mechanosensory hair cell death. *PLoS Genet.* **4**, e1000020.

Patra, C., Monk, K. and Engel, F. (2014). The multiple signaling modalities of adhesion G protein-coupled receptor GPR126 in development. *Receptors Clin Investig.* **1**, 79.

Patra, C., van Amerongen, M., Ghosh, S., Ricciardi, F., Sajjad, A., Novoyatleva, T., Mogha, A., Monk, K., Mühlfeld, C. and Engel, F. (2013). Organ-specific function of adhesion G protein-coupled receptor GPR126 is domain dependent. *Proc. Natl. Acad. Sci. USA* **110**, 16898-16903.

Pedregosa, F., Varoquaux, G., Gramfort, A., Michel, V., Thirion, B., Grisel, O., Blondel, M., Prettenhofer, P., Weiss, R., Dubourg, V., et al. (2011). Scikit-learn: Machine Learning in Python. *J. Mach. Learn. Res.* **12**, 2825−2830.

Pendleton, J. C., Shamblott, M. J., Gary, D. S., Belegu, V., Hurtado, A., Malone, M. L. and McDonald, J. W. (2013). Chondroitin sulfate proteoglycans inhibit oligodendrocyte myelination through PTPsigma. *Exp Neurol* **247**, 113-121.

Petersen, S., Luo, R., Liebscher, I., Giera, S., Jeong, S., Mogha, A., Ghidinelli, M., Feltri, M., Schöneberg, T., Piao, X., et al. (2015). The adhesion GPCR GPR126 has distinct, domain-dependent functions in Schwann cell development mediated by interaction with laminin-211. *Neuron* **85**, 755-769.

Poureetezadi, S., Cheng, C., Chambers, J., Drummond, B. and Wingert, R. (2016). Prostaglandin signaling regulates nephron segment patterning of renal progenitors during zebrafish kidney development. *Elife* **5**, pii: e17551.

Prasanna, X., Sengupta, D. and Chattopadhyay, A. (2016). Cholesterol-dependent Conformational Plasticity in GPCR Dimers. *Sci Rep* **6**, 31858.

Ravenscroft, G., Nolent, F., Rajagopalan, S., Meireles, A., Paavola, K., Gaillard, D., Alanio, E., Buckland, M., Arbuckle, S., Krivanek, M., et al. (2015). Mutations of GPR126 are responsible for severe arthrogryposis multiplex congenita. *Am J. Hum. Genet.* **96**, 955-961.

Rennekamp, A., Huang, X., Wang, Y., Patel, S., Lorello, P., Cade, L., Gonzales, A., Yeh, J., Caldarone, B., Roth, B., et al. (2016). σ1 receptor ligands control a switch between passive and active threat responses. *Nat. Chem. Biol.* **12**, 552-558.

Ricciardelli, C., Sakko, A. J., Ween, M. P., Russell, D. L. and Horsfall, D. J. (2009). The biological role and regulation of versican levels in cancer. *Cancer and Metastasis Reviews* **28**, 233-245.

Richter, S., Schulze, U., Tomançak, P. and Oates, A. (2017). Small molecule screen in embryonic zebrafish using modular variations to target segmentation. *2017* **8**, 1901.

Rogers, D. and Hahn, M. (2010). Extended-Connectivity Fingerprints. *J. Chem. Inf. Model.* **50**, 742–754.

Salzman, G., Zhang, S., Gupta, A., Koide, A., Koide, S. and Araç, D. (2017). Stachel-independent modulation of GPR56/ADGRG1 signaling by synthetic ligands directed to its extracellular region. *Proc. Natl. Acad. Sci. USA* **114**, 10095-10100.

Salzman, G. S., Ackerman, S. D., Ding, C., Koide, A., Leon, K., Luo, R., Stoveken, H. M., Fernandez, C. G., Tall, G. G., Piao, X., et al. (2016). Structural Basis for Regulation of GPR56/ADGRG1 by Its Alternatively Spliced Extracellular Domains. *Neuron* **91**, 1292-1304.

Schampel, A., Volovitch, O., Koeniger, T., Scholz, C. J., Jorg, S., Linker, R. A., Wischmeyer, E., Wunsch, M., Hell, J. W., Ergun, S., et al. (2017). Nimodipine fosters remyelination in a mouse model of multiple sclerosis and induces microglia-specific apoptosis. *Proc Natl Acad Sci U S A* **114**, E3295-E3304.

Shannon, P., Markiel, A., Ozier, O., Baliga, N., Wang, J., Ramage, D., Amin, N., Schwikowski, B. and Ideker, T. (2003). Cytoscape: A Software Environment for Integrated Models of Biomolecular Interaction Networks. *Genome Res.* **13**, 2498-2504.

Sharma, R., Wang, J. and Wu, Z. (1997). Mechanisms of inhibition of calmodulin-stimulated cyclic nucleotide phosphodiesterase by dihydropyridine calcium antagonists. *J. Neurochem.* **69**, 845-850.

Silver, J. and Miller, J. H. (2004). Regeneration beyond the glial scar. *Nat Rev Neurosci* **5**, 146-156.

Sriram, K. and Insel, P. (2018). G Protein-Coupled Receptors as Targets for Approved Drugs: How Many Targets and How Many Drugs? *Mol. Pharmacol.* **93**, 251-258.

Stoveken, H., Larsen, S., Smrcka, A. and Tall, G. (2018). Gedunin- and Khivorin-Derivatives Are Small-Molecule Partial Agonists for Adhesion G Protein-Coupled Receptors GPR56/ADGRG1 and GPR114/ADGRG5. *Mol. Pharmacol.* **93**, 477-488.

Subramani, R., Gonzalez, E., Nandy, S., Arumugam, A., Camacho, F., Medel, J., Alabi, D. and Lakshmanaswamy, R. (2017). Gedunin inhibits pancreatic cancer by altering sonic hedgehog signaling pathway. *Oncotarget* **8**, 10891-10904.

Tang, Y. D., Zheng, X. S., Ying, T. T., Yuan, Y. and Li, S. T. (2015). Nimodipine-mediated re-myelination after facial nerve crush injury in rats. *J Clin Neurosci* **22**, 1661-1668.

Thisse, C. and Thisse, B. (2008). High-resolution in situ hybridization to whole-mount zebrafish embryos. *Nat. Protoc.* **3**, 59-69.

Thompson, S., Wingrove, P., Connelly, L., Whiting, P. and Wafford, K. (2002). Tracazolate reveals a novel type of allosteric interaction with recombinant gamma-aminobutyric acid(A) receptors. *Mol. Pharmacol.* **61**, 661-669.

Tocci, G., Desideri, G., Roca, E., Calcullo, C., Crippa, M., De Luca, N., Gaudio, G., Lonati, L., Orselli, L., Scuteri, A., et al. (2018). How to Improve Effectiveness and Adherence to Antihypertensive Drug Therapy: Central Role of Dihydropyridinic Calcium Channel Blockers in Hypertension. *High Blood Press Cardiovasc Prev* **25**, 25-34.

Urban, N., Wang, L., Kwiek, S., Rademann, J., Kuebler, W. and Schaefer, M. (2016). Identification and Validation of Larixyl Acetate as a Potent TRPC6 Inhibitor. *Mol. Pharmacol.* **89**, 197-213.

Vettori, A., Greenald, D., Wilson, G., Peron, M., Facchinello, N., Markham, E., Sinnakaruppan, M., Matthews, L., McKeating, J., Argenton, F., et al. (2017). Glucocorticoids promote Von Hippel Lindau degradation and Hif-1α stabilization. *Proc. Natl. Acad. Sci. USA* **114**, 9948-9953.

Waller-Evans, H., Prömel, S., Langenhan, T., Dixon, J., Zahn, D., Colledge, W. H., Doran, J., Carlton, M. B., Davies, B., Aparicio, S. A., et al. (2010). The orphan adhesion-GPCR GPR126 is required for embryonic development in the mouse. *PLoS One* **5**, e14047.

Weininger, D. (1988). SMILES, a chemical language and information system. 1. Introduction to methodology and encoding rules. *J. Chem. Inf. Comput. Sci.* **28**, 31–36.

Weisman, J., Liou, A., Shelat, A., Cohen, F., Guy, R. and DeRisi, J. (2006). Searching for new antimalarial therapeutics amongst known drugs. *Chem. Biol. Drug Des.* **67**, 409-416.

Westerfield, M. (2000). *The zebrafish book. A guide for the laboratory use of zebrafish (Danio rerio)* (4 edn). Eugene: University of Oregon Press.

Whitfield, T. T., Granato, M., van Eeden, F. J. M., Schach, U., Brand, M., Furutani-Seiki, M., Haffter, P., Hammerschmidt, M., Heisenberg, C.-P., Jiang, Y.-J., et al. (1996). Mutations affecting development of the zebrafish inner ear and lateral line. *Development* **123**, 241-254.

Wight, T. N., Frevert, C. W., Debley, J. S., Reeves, S. R., Parks, W. C. and Ziegler, S. F. (2017). Interplay of extracellular matrix and leukocytes in lung inflammation. *Cell Immunol* **312**, 1-14.

Willett, P., Barnard, J. and Downs, G. (1998). Chemical Similarity Searching. *J. Chem. Inf. Comput. Sci.* **38**, 983–996.

Wootten, D., Christopoulos, A., Marti-Solano, M., Babu, M. and Sexton, P. (2018). Mechanisms of signalling and biased agonism in G protein-coupled receptors. *Nat. Rev. Mol. Cell Biol.* **19**, 638-653.

Yu, P., Hong, C., Sachidanandan, C., Babitt, J., Deng, D., Hoyng, S., Lin, H., Bloch, K. and Peterson, R. (2008). Dorsomorphin inhibits BMP signals required for embryogenesis and iron metabolism. *Nat. Chem. Biol.* **4**, 33-41.

Zada, D., Tovin, A., Lerer-Goldshtein, T. and Appelbaum, L. (2016). Pharmacological treatment and BBB-targeted genetic therapy for MCT8-dependent hypomyelination in zebrafish. *Dis Model Mech* **9**, 1339-1348.